Establishment and Control of Behavioral Bias in Drosophila Melanogaster

Permanent link

Terms of Use

Share Your Story

Establishment and Control of Behavioral Bias in *Drosophila melanogaster*

A dissertation presented

by

Kyobi Skutt-Kakaria

to

The Department of Molecular and Cellular Biology

in partial fulfillment of the requirements

for the degree of

Doctor of Philosophy

in the subject of Biochemistry

Harvard University

Cambridge, Massachusetts

April, 2018

Dissertation Advisor: Benjamin de Bivort   Kyobi Skutt-Kakaria

Establishment and Control of Behavioral Bias in *Drosophila melanogaster*

Abstract

Typically, variability observed across populations of animals is considered to be experimental
noise. However, it is clear that individuals display considerable idiosyncrasies in behavior that
are stable over both short and long time scales. Understanding how individuality arises and is
maintained within the nervous system is a major challenge in neuroscience.

I have found that biases in individuality in locomotor decision making are shaped during
development, especially during pupation. Disruption of normal synaptic partner matching
expands the magnitude of average locomotor biases in a population of flies. These biases are
the product of the motor system of the fly. A key pre-motor circuit in the brain, the central
complex, is likely to be a significant contributor to these biases. Using anatomical evidence from
extensive morphological studies performed by other groups, we modeled a core component of
this circuit and found that these deep brain neurons robustly form a ring attractor network under
a variety of parameters, providing evidence for this circuit as a tracking system of heading in the
fly. Finally, we have found that these locomotor biases are not as stable as previously thought,
they can be modulated by ambient luminance, being sometimes dramatically different in the
light and dark. This context dependence is mediated by vision and neurons within the central
complex, namely the same ring attractor network. Furthermore, we have found evidence that
output neurons of this network directly bias locomotor behavior due to asymmetric synaptic
output into a downstream area of the central complex, the lateral accessory lobe, in a context
dependent manner.

Table of Contents: Pg #

Introduction:

All animals, including humans, show substantial individuality across morphological traits. Variations in height, body mass or skin color are easily observed and can have significant effects on fitness (McKellar & Hendry 2009; Caumul & Polly 2009; Bubliy et al. 2001). However, an animal's individuality in decision making is arguably a more important trait, as it determines how one interacts with their environment and other animals of the same species (Cote et al. 2008; David et al. 2011; Sinn et al. 2006; Lichtenstein et al. 2017; Kain et al. 2015). Although behavior is often thought to be much more plastic than morphology, many studies suggest that personality traits can be largely genetically encoded (Bouchard et al. 1990; Nilsson et al. 2014; Bratko et al. 2017; Weiss et al. 2000). However, behavior is not fully explained by genetics and even identical twins raised in the same home can show dramatically different behavior from one another. Much of these differences have been explained through plasticity that reflects life history, however, a significant fraction of these likely arise from seemingly stochastic developmental processes (Freund et al. 2013; Honegger & de Bivort 2018). The brain could generate individuality through many different mechanisms, eventually being generated by differences in the physiology of neurons. Differences could include altered neuron excitability, synapse number, pre-synaptic vesicle density or post-synaptic receptor density, altered neurotransmitter balance or various glial cell related mechanisms. Indeed, differences are likely to be found across all the synapses in the brain as developmental processes are inherently noisy (Neves et al. 2004; Vogt et al. 2008). However, it could be the case that physiological differences at points of high convergence in the brain would be more likely to influence behavior. In this work, we have attempted to understand how individuality arises and is maintained within the brain of the fruit fly, *Drosophila melanogaster.* Specifically, we have investigated the role of a highly convergent deep brain area, the central complex, in establishing and reinforcing individuality in locomotor bias, a stable trait of individual flies.

There are several important advantages to using *Drosophila* to study individuality. First, its brain has sufficient numerical complexity so that individual neurons may have separable

roles in different behavioral processes; yet compact enough that those differences could be distributed over only a few neurons that may be easier to identify and observe. Second, *Drosophila* are easy to rear in nearly identical conditions to minimize environmental effects on each individual's development. Third, they are small enough to be appropriate for high-throughput behavioral assays, a requirement for quantifying distributions of behavior (Buchanan et al. 2015; Branson et al. 2009). Finally, in *Drosophila* we have access to sparse neural populations with genetic tools that allow for perturbation and characterization of specific neurons (Jenett et al. 2012; Pfeiffer et al. 2008). Taking advantage of all these qualities of *Drosophila,* we can begin to probe for locations in the brain where individuality in behavior can arise.

In *D. melanogaster,* sensory information is collected by primary sensory organs for vision on the head and taste and smell on the head and legs. In addition, flies have extensive touch receptors distributed across the cuticle (Zhu 2013; Couto et al. 2005; Tuthill & Wilson 2016). The best characterized sensory system in flies is vision. The eyes of the fly are an arrangement of ~800 ommatidia on each side with 8 photoreceptor cells in each ommatidia. Six of the photoreceptors have been shown to broadly respond to light at frequencies that span the visual spectrum. These photoreceptors primarily mediate motion vision, edge detection and luminance detection (Borst et al. 2010). The last two photoreceptors have chromatic responses and are important in color vision (Lin et al. 2016). Photoreceptor responses are propagated through the multiple layers of the optic lobes where increasingly complex features of the visual environment are extracted and integrated and likely encounter self-motion cancelation and perhaps multi-modal integration in a set of optic glomeruli along the lateral edge of the central brain (A. J. Kim et al. 2015; Aptekar et al. 2015). Neurons encoding these higher order features then project to deeper brain areas (Mu et al. 2012). As these signals are propagated they are likely to become integrated with other features of both vision and other sensory modalities as well as internal states.

The activity in these deep brain interneurons must somehow be used to guide adaptive behavior. A central deep brain pre-motor area in the *Drosophila* brain is the central complex.

The central complex is a highly structured deep brain area that is clustered around the middle of the brain, spanning the midline. The central complex tracks spatial information and has been shown to be involved in many tasks, especially those involving both sensory and spatial systems (Martin et al. 2015; Varga et al. 2017; Turner-Evans & Jayaraman 2016). The central complex is composed of four main neuropil, the protocerebral bridge (PB), ellipsoid body (EB), fan-shaped body (FB) and paired noduli. Each of these neuropil are organized in a columnar and tangential arrangement of input neurons that are spatially segregated from their neighbors, with the notable exception of the noduli. This organization is thought to underlie the ability of the central complex to maintain spatial information about the world around the fly. Interestingly, output neurons of the central complex are no longer columnar, perhaps indicating that the information carried by those neurons is no longer spatially separated. The central complex receives projections from thousands of input neurons that encode diverse sensory information. Surprisingly however, it projects only a few dozen output neurons into the gall and lateral accessory lobe. Because the central complex has significant convergence into a small number of output neurons, it is a great location to investigate a mechanistic origin of individually stable behavioral biases as differences in those neurons would not be averaged out across the population as easily and could propagate downstream into the pre-motor regions of the brain.

Neurons in the central complex and associated neuropil influence diverse motor behaviors in the fly (Cande et al. 2018). Anatomical studies suggest that these areas do not directly influence behavior but may instead project to upper motor neurons in the several pre-motor areas of the ventral brain that send descending interneurons into the ventral nerve cord, the insect equivalent of the spinal cord, to direct muscle activation in the lower body segments (Hsu & Bhandawat 2016; Namiki et al. 2017). Optogenetic activation screens have shown that some descending neurons in the central brain can deterministically trigger behaviors. However, the majority of descending neurons do not show clear one to one behaviors when activated, meaning that the descending neurons are likely to act in concert to trigger distinct behaviors (Robie et al. 2017).

Fruit flies display a wide range of interesting behaviors that are likely to have individual tendencies such as odor and taste preferences, likelihood to court, probability to behave aggressively, propensity to seek out light etc. Many of these behavioral preferences are effected by neural adaptation making individual preferences more difficult to estimate. Therefore, in this work we have focused on a behavioral individuality that doesn't show any evidence of adaptation: locomotor handedness (Buchanan et al. 2015; Ayroles et al. 2015). When locomoting, individual flies show tendencies to walk in one direction or another. Most flies tend to walk to the left or right with equal probability. However some animals are strongly biased to the right or left. Mutations of the central complex can modulate how much variability in locomotor biases are seen in a population. Furthermore, when certain neurons innervating the PB of the central complex were silenced using the temperature-sensitive dynamin mutant, Shibire^{ts}, the extremity of individual turn biases could be acutely increased (lefties became more lefty or vice versa). This indicates that the PB, and the central complex by extension, has a role in controlling the magnitude of locomotor bias individuals display (Buchanan et al. 2015).

In this work we have investigated several hypotheses regarding the neural development and control of individual locomotor biases. First, we investigated the genetic determinants that affect the distribution of individual locomotor biases using a genome-wide association approach and we have shown that a particular trans-synaptic targeting protein, teneurin-a, is important for establishing the distribution of individual locomotor biases. Second, we have investigated the role of the PB to EB recurrent circuitry in tracking locomotor heading by modeling the activity dynamics of that brain area. By modeling all of the neurons of the PB as integrate-and-fire units and assuming all-to-all connectivity from known light level innervation patterns, we found that the neurons connecting the PB and EB robustly behave as a ring-attractor circuit even with significant changes to individual synapse weights. Finally, we have investigated the role of sensory modulation of individual locomotor biases to identify loci of locomotor individuality. By changing ambient luminance conditions, we have found that individual animals can display dramatically different turn biases in the light and dark. Furthermore, we have found that these

4

differences arise in the central complex and that asymmetric neuronal morphology in projection neurons out of the central complex predicts those differences.

Aptekar, J.W. et al., 2015. Neurons forming optic glomeruli compute figure-ground discriminations in Drosophila. *The Journal of neuroscience : the official journal of the Society for Neuroscience*, 35(19), pp.7587–7599.

Ayroles, J.F. et al., 2015. Behavioral idiosyncrasy reveals genetic control of phenotypic variability. *Proceedings of the National Academy of Sciences of the United States of America*, 112(21), pp.6706–6711.

Borst, A., Haag, J. & Reiff, D.F., 2010. Fly Motion Vision. *Annual Review of Neuroscience*, 33, pp. 49-70

Bouchard, T.J. et al., 1990. Sources of human psychological differences: the Minnesota Study of Twins Reared Apart. *Science (New York, N.Y.)*, 250(4978), pp.223–228.

Branson, K. et al., 2009. High-throughput ethomics in large groups of Drosophila. *Nat Methods*, 6(6), pp.451–457.

Bratko, D., Butković, A. & Vukasović Hlupić, T., 2017. Heritability of Personality. *Psihologijske teme*, 26(1), pp.1–24.

Bubliy, O.A., Loeschcke, V. & Imasheva, A.G., 2001. Genetic variation of morphological traits in *Drosophila melanogaster* under poor nutrition: isofemale lines and offspring–parent regression. *Heredity*, 86(3), p.363.

Buchanan, S.M., Kain, J.S. & de Bivort, B.L., 2015. Neuronal control of locomotor handedness in Drosophila. *Proceedings of the National Academy of Sciences of the United States of America*, 112(21), pp.6700–6705.

Cande, J. et al., 2018. Optogenetic dissection of descending behavioral control in Drosophila. *bioRxiv*, p.230128.

Caumul, R. & Polly, P.D., 2005. Phylogenetic And Environmental Components Of Morphological Variation: Skull, Mandible, And Molar Shape In Marmots (Marmota, Rodentia). *Evolution*, 59(11), pp. 2460-72

Cote, J., Dreiss, A. & Clobert, J., 2008. Social personality trait and fitness. *Proceedings of the Royal Society of London B: Biological Sciences*, 275(1653), pp.2851–2858.

Couto, A., Alenius, M. & Dickson, B.J., 2005. Molecular, Anatomical, and Functional Organization of the Drosophila Olfactory System. *Current Biology*, 15(17), pp.1535–1547.

David, M., Auclair, Y. & Cézilly, F., 2011. Personality predicts social dominance in female zebra finches, Taeniopygia guttata, in a feeding context. *Animal Behaviour*, 81(1), pp.219–224.

Freund, J. et al., 2013. Emergence of Individuality in Genetically Identical Mice. *Science* 340(6133), pp.756–759.

Green, J. et al., 2017. A neural circuit architecture for angular integration in Drosophila. *Nature*. 546, pp. 101-106

Honegger, K. & de Bivort, B., 2018. Stochasticity, individuality and behavior. *Curr Biol*, 28(1), pp.R8–R12.

Hong, W., Mosca, T.J. & Luo, L., 2012. Teneurins instruct synaptic partner matching in an olfactory map. *Nature*, 484(7393), pp.201–207.

Hsu, C.T. & Bhandawat, V., 2016. Organization of descending neurons in Drosophila melanogaster. *Scientific reports*. 6, 20259

Jenett, A. et al., 2012. A GAL4-driver line resource for Drosophila neurobiology. *Cell reports*, 2(4), pp.991–1001.

Kain, J. et al., 2015. Bet-hedging, seasons and the evolution of behavioral diversity in Drosophila. *Evolution,* 69-12: 3171-3185

Kim, A.J., Fitzgerald, J.K. & Maimon, G., 2015. Cellular evidence for efference copy in Drosophila visuomotor processing. *Nat Neurosci*, 18(9), pp.1247–1255.

Kim, S.S. et al., 2017. Ring attractor dynamics in the Drosophila central brain. *Science (New York, N.Y.)*, 356(6340), pp.849–853.

Kohsaka, H. et al., 2012. Development of larval motor circuits in Drosophila. *Development, growth & differentiation*, 54(3), pp.408–419.

Lichtenstein, J.L.L. et al., 2017. Intraindividual Behavioral Variability Predicts Foraging Outcome in a Beach-dwelling Jumping Spider. *Scientific reports*, 7(1), p.18063.

Lin, T.-Y. et al., 2016. Mapping chromatic pathways in the Drosophila visual system. *J Comp Neurol* 524(2), pp.213-27.

Martin, J.P. et al., 2015. Central-Complex Control of Movement in the Freely Walking Cockroach. *Current Biology*, 25(21), pp. 2795-2803

McKellar, A.E. & Hendry, A.P., 2009. How Humans Differ from Other Animals in Their Levels of Morphological Variation. *PLOS One*, 4(9), p.e6876.

Mosca, T.J. & Luo, L., 2014. Synaptic organization of the Drosophila antennal lobe and its regulation by the Teneurins. *eLife*, 3:e03726

Mu, L. et al., 2012. Optic Glomeruli and Their Inputs in Drosophila Share an Organizational Ground Pattern with the Antennal Lobes. *The Journal of neuroscience : the official journal of the Society for Neuroscience*, 32(18), pp.6061–6071.

Namiki, S. et al., 2017. The functional organization of descending sensory-motor pathways in Drosophila. *bioRxiv*, p.231696.

Neves, G. et al., 2004. Stochastic yet biased expression of multiple Dscam splice variants by individual cells., *Nature Genetics* 36(3), pp.240–246.

Nilsson, J.Å. et al., Individuality in movement: The role of animal personality, ISBN: 9780199677184

Pfeiffer, B.D. et al., 2008. Tools for neuroanatomy and neurogenetics in Drosophila., *PNAS* 105(28), pp.9715–9720.

Robie, A.A. et al., 2017. Mapping the Neural Substrates of Behavior. *Cell*, 170(2), pp.393–406.e28.

Seelig, J.D. & Jayaraman, V., 2015. Neural dynamics for landmark orientation and angular path integration. *Nature*, 521(7551), pp.186–191.

Sinn, D.L., Apiolaza, L.A. & Moltschaniwskyj, N.A., 2006. Heritability and fitness–related consequences of squid personality traits. *Journal of Evolutionary Biology*, 19(5), pp.1437–1447.

Spindler, S.R. & Hartenstein, V., 2010. The Drosophila neural lineages: a model system to study brain development and circuitry. *Development Genes and Evolution*, 220(1-2), pp.1–10.

Turner-Evans, D.B. & Jayaraman, V., 2016. The insect central complex. *Curr Biol*, 26(11), pp.R453–7.

Tuthill, J.C. & Wilson, R.I., 2016. Mechanosensation and Adaptive Motor Control in Insects. *Current Biology*, 26(20), pp.R1022–R1038.

Varga, A.G. et al., 2017. Spatial Navigation and the Central Complex: Sensory Acquisition, Orientation, and Motor Control. *Frontiers in Behavior Neuroscience*, 11:4

Vogt, G. et al., 2008. Production of different phenotypes from the same genotype in the same environment by developmental variation. *Journal of Experimental Biology*, 211(Pt 4), pp.510–523.

Weiss, A., King, J.E. & Figueredo, A.J., 2000, The Heritability of Personality Factors in Chimpanzees (Pan troglodytes). *Behavior Genetics*, 30(3), pp.213–221.

Wolff, T., Iyer, N.A. & Rubin, G.M., 2015. Neuroarchitecture and neuroanatomy of the Drosophila central complex: A GAL4-based dissection of protocerebral bridge neurons and circuits. *Journal of Comparative Neurology*, 523(7), pp.997–1037.

Zhu, Y., 2013. The Drosophila visual system. *Cell Adhesion & Migration*. 7(4), pp. 333-344

Page was left intentionally blank

Chapter I: Behavioral idiosyncracy reveals genetic control of phenotypic variability

Abstract:

Quantitative genetics has primarily focused on describing genetic effects on trait means and largely ignored the effect of alternative alleles on trait variability, potentially missing an important axis of genetic variation contributing to phenotypic differences among individuals. To study the genetic effects on individual-to-individual phenotypic variability (or intragenotypic variability), we used a panel of *Drosophila* inbred lines and measured the spontaneous locomotor behavior of flies walking individually in Y-shaped mazes, focusing on the variability in locomotor handedness (left-right turning bias), an assay optimized to measure variability. We discovered that some lines had consistently high levels of intragenotypic variability among individuals while lines with low variability behaved as though they tossed a coin at each left/right turn decision. We demonstrate that the degree of variability is itself heritable. Using a genome-wide association study (GWAS) for the degree of intragenotypic variability as the phenotype across lines, we identified several genes expressed in the brain that affect variability in handedness without affecting the mean. One of these genes, *Ten-a* implicates a neuropil in the central complex of the fly brain as influencing the magnitude of behavioral variability, a brain region involved in sensory integration and locomotor coordination. We have validated these results using genetic deficiencies, null alleles, and inducible RNAi transgenes. Our study reveals the constellation of phenotypes that can arise from a single genotype and shows that different genetic backgrounds differ dramatically in their propensity for phenotypic variabililty. Because traditional mean-focused GWA studies ignore the contribution of variability to overall phenotypic variation, current methods may miss important links between genotype and phenotype.

Introduction:

Quantitative genetics was founded on the assumption that phenotypic variation is explained solely by differences in mean phenotypes among genotypes. Under this model, intragenotypic variability is assumed to be attributable to non-genetic environmental perturbations (1). There is

however, growing evidence for the importance of genetic control of variance (2, 3, 4) and that variance itself is a quantitative trait. Although studies of morphology (5, 6, 7) and animal breeding (8, 9) have long noted the heterogeneity of variance among genotypes, this axis of variation has received little attention compared to the effect of genetic variation on trait means. As a result, the mechanisms by which variable phenotypes arise from a uniform genetic background are still poorly understood, particularly in the context of behavior, where variability may be a critical determinant of phenotypic differences (10, 11). Most recently, with the advent of genome-wide association studies, several groups (3, 4, 12,13) have mapped quantitative trait loci affecting variance (vQTLs) by comparing phenotypic variances among individuals that share alleles. These studies examine the average effect of QTL alleles across genetic backgrounds and heterogeneous environments across individuals (14), in the process losing any specific effects intrinsic to each individual.

Here, we examine diversity that is typically hidden in population averages, by examining phenotypic variability among individuals with the same genotype. This is the variation that we would observe if we could generate a large number of copies of individuals of the same genotype in a common environment, and measure a trait across them (an experiment for which isogenic lines (15, 5, 6, 7, 14) are especially suited). In this case, phenotypic differences among genetically identical individuals result from subtle micro-environmental perturbations and stochasticity in development, whereas differences in variability among genotypes reflect genetic differences in developmental stability (7). Although intragenotypic variability contributes to phenotypic variation in a population, this source of variation is not usually estimable because, with few exceptions, each individual in an outbred diploid population is a unique instance of its genotype (Fig. 1A). As a consequence we have little understanding of the causes and consequences of inter-individual intragenotypic variability. This phenotypic variance nevertheless has wide ranging implications. In evolutionary biology, variability offers an adaptive solution to environmental changes (15, 16). In medical genetics, many diseased states emerge
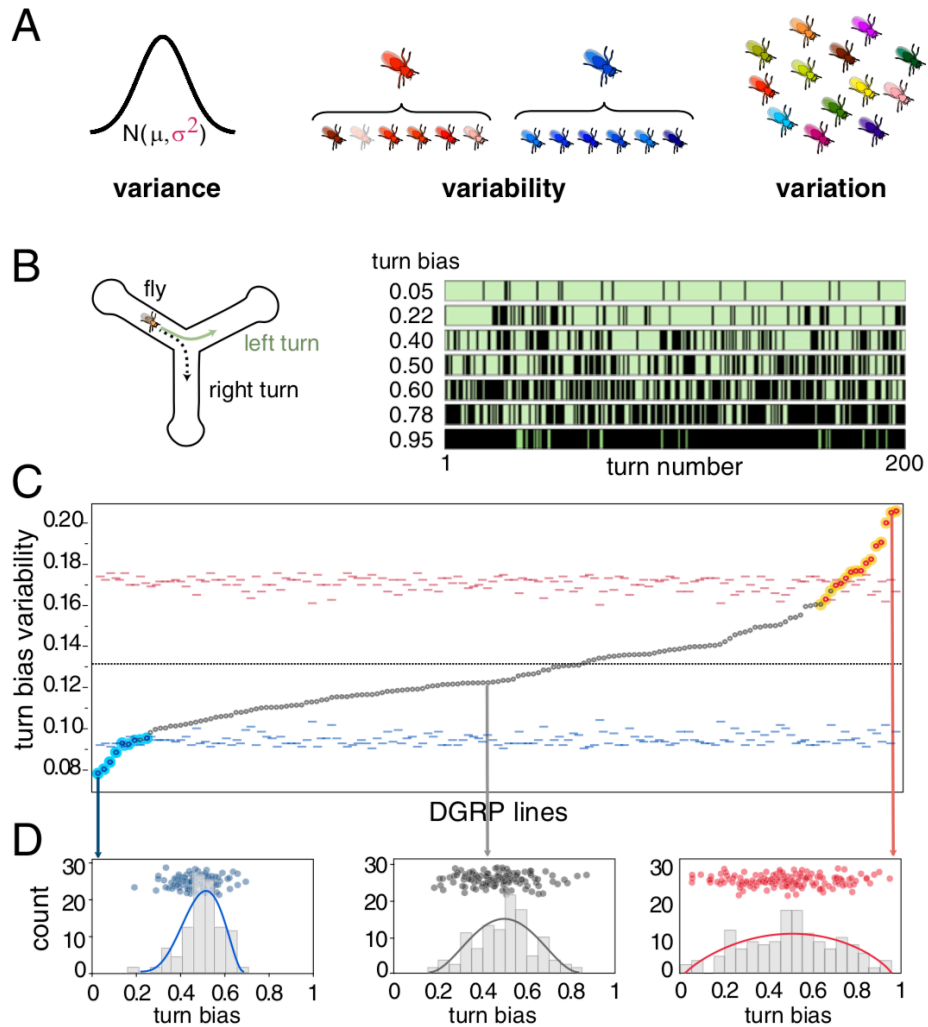
Fig. 1: Intragenotypic variability of locomotor handedness varies across DGRP lines.

A. The similarity between concepts of variance, variation and variability may lead to some confusion. Variance is used to describe the standard statistical dispersion parameter (σ^2) or estimates of it derived from observations (s^2). Variability refers to the potential of an organism or genotype to vary phenotypically, phenotypic differences we could observe across clones of the same genotype. For example (i.e., red fly = high variability genotype, blue fly = low variability genotype). Variation refers to the realized (observable) differences between individuals or genotypes. **B**. Diagram of the Y-maze used to quantify individual locomotor behavior. Plot at right illustrates 200 sequential turns for 7 representative individual flies. A turn bias of 0.05 indicates that this particular fly turned right 5% of the time (black stripes indicate right turns and green stripes left turns). **C**. Sorted distribution of the standard deviations of within-line individual turn bias, for 159 DGRP lines. Red and blue filled dots are significant, exceeding their corresponding tick-marked 99.9% confidence intervals, estimated by permutation. See table S1 for experimental sample sizes. Cyan and yellow highlighted dots are significant at $p < 0.001$ based on non-parametric bootstrap. **D**. Distributions of turning bias across individuals for three representative DGRP lines with low, intermediate and high intragenotypic variability. Each dot represents the turning bias of a single fly within that line. Lines are beta distribution fits, chosen because they model over-dispersed binomial distributions.

beyond a phenotypic threshold, and high variability genotypes will produce a larger proportion of individuals exceeding that threshold than low variability genotypes, even if each genotypic class has the same mean. While intragenotypic variability has been discussed in animal behavior, particularly in the context of the emergence of personality (10, 17), to date no genes have been associated with behavioral variability that do not also affect the mean.

To study phenotypic variability, we used a panel of wild-derived *Drosophila* inbred lines (21). These are an ideal tool because the genetic variation that was present between individual flies in their natural population is now captured between lines in the panel. For each line, this allows us to measure any phenotype on a large number of individuals of the same genetic background, age, and rearing environment, thus empirically estimating the magnitude of intragenotypic variability (Fig. 1A). Specifically, we measured the spontaneous locomotor behavior of flies walking individually in Y-shaped mazes (18), focusing on the variability in locomotor handedness (left-right turning bias). The precision and high-throughput nature of our assays allows a large number of flies to be measured per genotype and permits robust estimates of the sampling error on variance itself.

Results:

We tracked two hours of locomotor behavior of 110 individuals (on average) from each of 159 lines from the *Drosophila* Genetic Reference Panel (DGRP) in a randomized block design. For each individual fly, we recorded the time and left-right direction of each turn in the maze (Fig. 1B), estimating a turn bias score as the fraction of turns that were to the right. Flies performing more than 50 turns were analyzed, and completed 413 turns per trial on average. We began by comparing the mean turning bias and found no significant genetic variation across lines (Fig. S1). In other words, averaged across individuals *within* a line, each line is unbiased, making an equal proportion of left and right turns (with the modal fly being unbiased – Fig 1). We verified the lack of genetic variation for turning bias *within* lines by crossing pairs of males
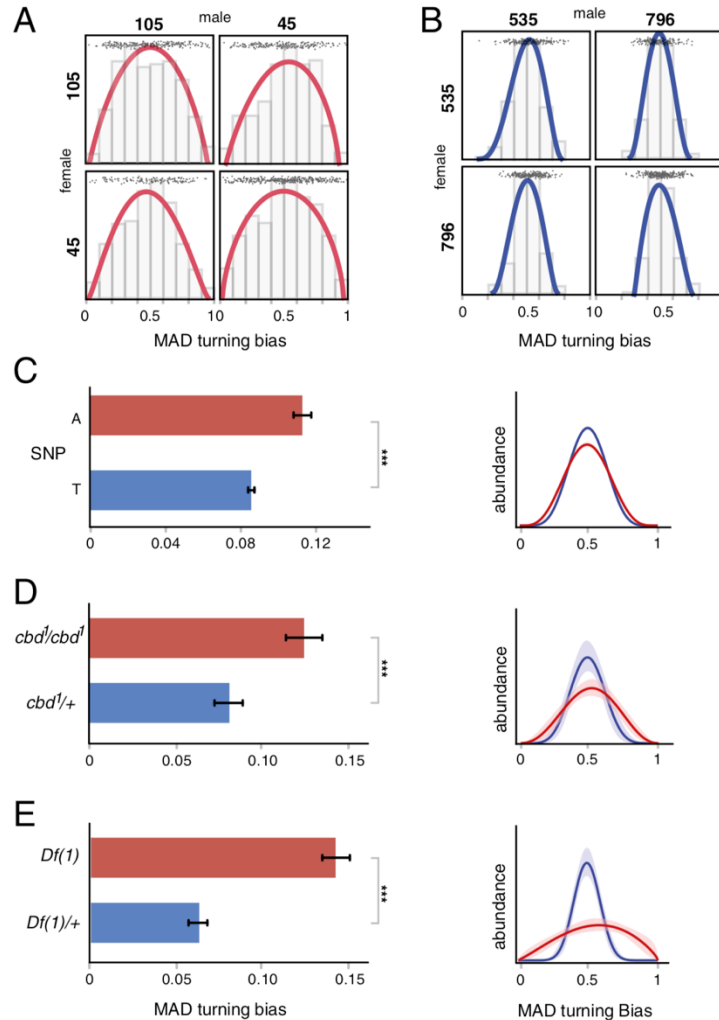
15

Fig. 2: Intragenotypic variability for turning bias is heritable. Effect of *Ten-a* mutation on intragenotypic variability.

A. Distribution of F1 turn biases resulting from high variance line 105 reciprocally crossed to high variance line 45 (Brown-Forsythe *p* = 0.08*;* $n_{105x105}$ = 235; $n_{45x45;}$ = 315; n_{105*45} = 223; n_{45*105} = 135). **B**. Distribution of F1 turn biases resulting from low variance line 535 reciprocally crossed to low line variance line 796 (Brown-Forsythe *p* = 0.02; $n_{535x535}$ = 197 $n_{796x796}$ = 265; $n_{796*535}$ = 160; $n_{535*796}$ = 234). In both panels, the progeny are presented on the off diagonal. Lines are beta distribution fits. Points are individual flies. For both 2A. and 2B. *p*-values comparing F1 to parents ranged form 0.14 to 0.99, uncorrected for multiple comparisons. **C**. Intragenotypic variability (MAD) in turn bias of flies harboring alternative alleles of the *Ten-a* SNP identified in our GWAS (*n* = 159, GWAS *p* < 3 × 10^{-6}; phenotypic variance explained by this polymorphism: R-square = 19.5%). **D**. Turn bias MAD of a homozygous *Ten-a* null allele (*cbd¹*; red) and heterozygous control (blue). *bk* indicates the *Ten-a⁺* genetic background Berlin-K. $n_{cbd1/bk}$ = 59, $n_{cbd1/cbd1}$ = 99, Brown-Forsythe *p* = 0.0074, bootstrapping *p* < 0.001. **E**. Turn bias MAD of a line bearing a homozygous deficiency overlapping *Ten-a* (red) and heterozygous control (blue). $n_{Df(1)-bk}$ = 100, $n_{Df(1)Ten-a}$ = 97, Brown-Forsythe *p* = 1.5^{-11}, bootstrapping *p* < 0.001. *** *p* < 0.001. Right plots in all panels are corresponding beta distribution fits of the distribution of turn bias scores within each experimental group. Shaded regions are 95% CIs on the beta fits, estimated by bootstrap resampling; CIs in (*a*) small compared to line thickness. Error bars are +/- one standard error estimated by bootstrap resampling.

and females with matched turning biases (*e.g.,* two strongly right-biased parents). For all crosses, the phenotypic mean and variance of the distribution of the F_1 generation was statistically indistinguishable from the distribution of the parental line (Fig. S2). Handedness therefore provides an ideal framework to study the genetics of variability because genetic effects on variability are not confounded by mean effects.

Next, using parametric (ANOVA) and non-parametric (bootstrapping) statistical approaches, we compared levels of intragenotypic variability across lines and found highly significant among-line differences in variability, implying that the abundance of individuals that were either strongly left- or right-biased was itself variable among lines. This indicates that the degree of intragenotypic variability itself is under genetic control in these lines (Fig. 1C, Table S1). In order to obtain further evidence that intragenotypic variability is heritable, we mated two high-variance and two low-variance lines to each other and measured turning bias in the resulting progeny (phenotyping an average of 183 individuals per cross). Intercrosses between high-variance lines led to high variance F_1 progeny and crosses with low-variance lines yielded low variance F_1 progeny (Fig. 2A-B). In both cases the variability in the F_1 progenies was statistically indistinguishable from that of the parents.

It is conceivable that some lines might be better than others at buffering micro-environmental perturbations, in which case the degree of intragenotypic variability among lines would be correlated across traits. To test this possibility, we scored additional phenotypes from our Y-maze data, namely, the total number of turns (a measure of overall activity); the left-right mutual information between successive turns; and the regularity of turn timing. We also analyzed other phenotypes previously measured on the DGRP at the individual level (starvation resistance (19), chill coma recovery (19), startle response (19), and night sleep (20)). We found significant genetic variation for variability in all these phenotypes, confirming that genetic control of variability is ubiquitous across phenotypes. On the other hand, we found no evidence that the

17
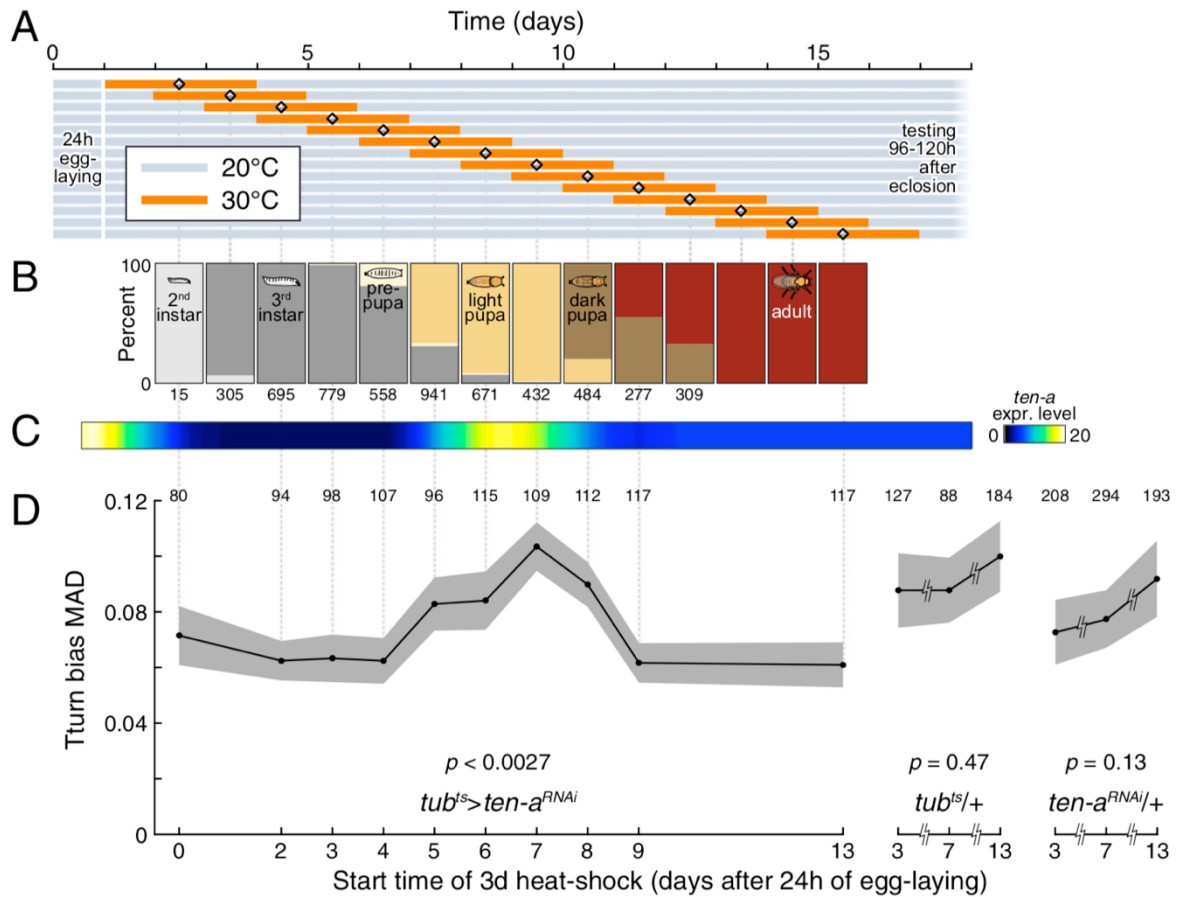
Fig. 3: Disruption of *Ten-a* expression in mid-pupa affects behavioral variance.
A. Time-courses of sliding window *Ten-a* RNAi induction. Flies laid eggs for 24 h prior the start of the experiment and were reared at 20°C (gray) until three days of RNAi induction at 30°C (orange). Flies were then returned to 20°C until they were tested 3 to 5 days post-eclosion. **B**. Fraction of flies at any developmental stage during the course of the experiment. Numbers indicate sample sizes. **C**. *Ten-a* expression level over development. Expression level derived from modENCODE. **D**. Effect of temperature inducible *Ten-a* RNAi on the variability of turning bias over development. Knock down effect varied significantly with the timing of the induction window ($p = 0.0027$) estimated by a bootstrapping omnibus test (see Supplementary materials), with a knock down starting on day 7 greatly increasing variability. This knockdown window coincides with the peak of *Ten-a* expression during pupation. Grey regions represent +/- standard error, estimated by bootstrapping. To the right, the controls, *tub^ts*/+ and *Ten-a^RNAi*/+, measured after 3 day 30°C windows starting on days 3, 7 and 13, show no effect ($p < 0.47$ and $p < 0.13$ respectively). Numbers above data indicate sample sizes. Vertical guide lines associate data points across panels.

18

variances of these traits are correlated across phenotypes (with the sole exception of mean absolute deviations (MAD) of turn bias and switchness) (Fig. S3). This suggests that the genetic basis for intragenotypic variability is trait-specific (and implicates many independent loci controlling these often-ignored traits).

The DGRP lines have been fully sequenced (19), allowing for genome wide association mapping using the variability (i.e. MAD) of turning bias as a trait. While the DGRP is underpowered to study the architecture of complex traits due to the relatively small number of lines (n = 159 in our study), it is a good resource to identify candidate genes for experimental follow up (21, 22). To that end, we performed an association study using a series of locus-specific mixed linear models (accounting for relatedness between lines as well as experimental block effect) and found 36 polymorphisms in 22 genes associated with variability in turning bias using a nominal p-value (21, 19) of 5 x 10^{-6} (Table S2). These genes are enriched with high significance for expression in the central nervous system both in adults and in larvae (adult CNS enrichment in adult Fisher Exact Test p < 0.001 and in larvae Fisher Exact Test p < 0.01, data from FlyAtlas (23)). Among these, the synaptic target recognition gene *Tenascin accessory* (*Ten-a,* GWAS $p < 3 \times 10^{-6}$) (Fig. 2C) caught our attention. Ten-a is a transmembrane signaling protein involved in synapse formation (24, 25), typically expressed pre-synaptically. In the antennal lobe Ten-a supports an expression-level matching code with high-expression neurons partnering with other high expression neurons (and low with low) (26). Teneurin impairment causes profound neuromuscular junction disruption (27). Within the central brain, Ten-a mutation causes midline fusion defects within the central complex), a brain structure implicated in sensory integration and locomotion 4-6, 28). *Ten-a* is highly conserved from insects to mammals (29).In order to validate the role of *Ten-a* in modulating variability in turning bias, we used a null allele (*Ten-a*[cbd-KS96]) (Fig. 2D), a deficiency overlapping *Ten-a* (*Df(1)Ten-a* (22) (Fig. 2E)), and expression knock-down using inducible RNAi (tub-Gal4;tub-Gal80[ts] > UAS-TRiP.JF03375) (Fig. 3). In all cases, disrupting *Ten-a* increased the variability in turning bias

with no effect on the mean. The effect of RNAi knock-down suggests a quantitative relationship between *Ten-a* mean expression and variance in turning bias.

The bias in handedness of a given fly is a fixed property of that individual (*e.g.* a young adult with a strong left bias will display this bias throughout its life (18)). This suggests that handedness may be wired during development. To determine if there is a critical developmental period when *Ten-a* expression is required to regulate variability, we used temperature-inducible RNAi to knock down *Ten-a* in sliding 3-day windows (Fig. 3A and B). We found that knocking down *Ten-a* expression in mid-pupae increases the resulting adults' variability (Fig. 3D). This stage coincides with a spike in *Ten-a* expression (Fig. 3C) and the formation of the central complex (26).

Discussion:

In this study we have used a simple behavioral trait to show that individual genotypes vary considerably in their degree of intragenotypic variability (15, 7), and found that this variation is heritable. Similar to work on fluctuating asymmetry (30), such experiments allow us to estimate how robust development is to micro-environmental perturbation and highlight the consequences of this variation for an *individual*'s phenotype. Our use of inbred lines enables the estimation of a parameter (intragenotypic variability) that otherwise could not be observed and uncovers the spectrum of phenotypes a given genotype can produce in a given environment. Futher, using association mapping uncovered a gene , ten-a, which implicating the central complex of the brain.

In a companion study, Buchanan *et al* (18) mapped a set of neurons within the central complex (*i.e.* protocerebral bridge columnar neurons) that regulates the magnitude of left-right turn bias, and therefore the magnitude of intragenotypic variability. Together these studies constitute a rare example

linking natural genetic variation for a complex behavioral trait, to mutants implicating a brain region, to a specific sub-circuit within this region. Thus we can begin to paint the path from genetic variation to behavioral individuality.

One of the great challenges in modern biology is to understand the functional consequences of genomic variation and to determine how and when it contributes to phenotypic differences among individuals. During the past decade, we have made remarkable progress in understanding the genetic basis of complex traits and diseases, thanks in part, to the application of GWAS to large cohorts. Unfortunately, we have fallen short of the goal of explaining heritability for complex traits in terms of allelic effects (31, 32). The traditional framework used to map QTLs focuses on the average effect of alternative alleles averaged in a population. However, as we have shown in this study, when phenotypic variation results from alleles that modify phenotypic variance rather than the mean, this link between genotype and phenotype will be not be detected. The case of locomotor handedness is an extreme example, where there is virtually no heritability for mean handedness and all the phenotypic variation in this population is attributable to intragenotypic variability. Nevertheless, it highlights the important contribution genetic control of variability can play in our understanding of the cause of phenotypic variation.

If, in a common macro-environment, different genetic backgrounds vary in their propensity for phenotypic variability, individuals drawn from a high-variability genetic background have the potential to explore a wider range of phenotypic space than those drawn from a low-variability background (sometimes far beyond what may be determined by the mean effect alone). We observe intragenotypic variability for every phenotypes we have investigating, ranging from behavioral to metabolic, indicating that variability is ubiquitous. This could be advantageous in the context of evolutionary adaptation, but in human genetics it could be deleterious when an extreme phenotype enhances disease risk. The implications for medical genetics are far-reaching (31, 32, 14), specifically for attempts to predict phenotypes from

21
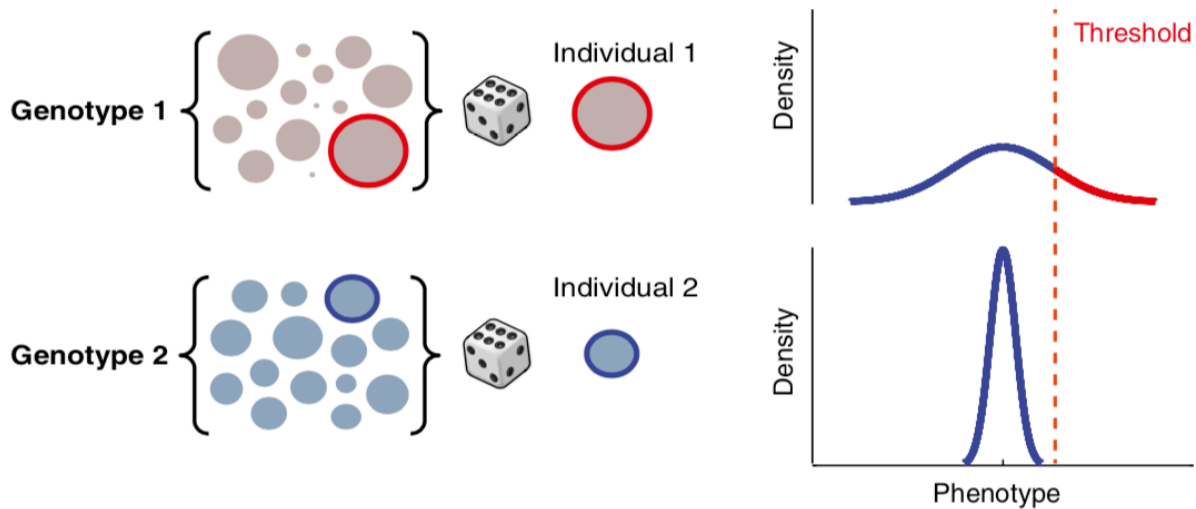
Fig. 4: Consequences of intragenotypic variability on the fraction of a hypothetical population exceeding a disease threshold.

Visual representation of the effects of variance on the prevalence of phenotypes exceeding a threshold, such as a disease state. Genotype 1 and 2 differ in their degree of intragenotypic variability. The sets of circles at left represent the range of possible outcomes for each genotype. Generally, each individual in an outbred diploid organism is a unique instance of its genotype. By contrast, our experiments with inbred lines allow us to consider multiple individuals from the same distribution. An individual drawn at random from genotype 1 (high variability) may land in the tail of the distribution, potentially in disease space. On the other hand an individual drawn randomly from genotype 2 never gets a chance to explore the phenotypic space explored by genotype 1, even if it is just as much of an outlier within its respective distribution.

genotypes. This point is illustrated in Fig. 4: if we consider that each individual is a random draw from a distribution determined (in part) by its genotype, then we should not think of genotypes as determining the phenotypic value of that individual, rather, we should think of genotypes as determining the *probability* of that individual having a particular phenotypic value (33). This model requires the development of additional experimental and statistical approaches for mapping QTLs and several are already being developed (e.g., 33, 12, 14, 4, 34, 39, 40) .

Our work does not address the adaptive significance of intragenotypic variability or the evolutionary forces driving variation at alleles affecting variability. This would, for example, require additional information on the fitness consequences of variability in handedness. Although the allele frequencies of the most significant SNPs are relatively high in the DGRP, we did not detect any significant deviation from neutrality for the genes harboring these SNPs. It should also be emphasized that differences in variability across lines could emerge from a neutral process. The nature of the forces influencing the evolution of alleles that affect variability has, more generally, been the focus of a rich theoretical literature explaining this phenomenon from a game theory perspective (41) or in terms of bet-hedging (42). Under various scenarios, increased phenotypic variability may allow some individuals in a population to explore a broader range of phenotypic space, thus maintaining this population at, or close to, some fitness optimum over time. This should be particularly true in fluctuating environments (43, 44). We point out however that it is still an open question whether genetic mechanisms leading to variation in intragenotypic variability are also associated with those underlying phenotypic plasticity (i.e. genotype-by-environment interactions in response to macro-environmental variation, described for example through reaction norms).

While inbred lines are an ideal way to study the genetic basis of intragenotypic variability (since variation between individuals within a line is cause primarily by micro-environmental effects), not all systems are amenable to this approach. In many circumstances, alternate designs are available. For example, if the phenotype of interest is molecular, recent progress in single-cell technology now makes it possible to measure cell to cell variation within an individual genotype (14), enabling the study of intragenotypic variability in natural populations, including humans (33). At the organismal level, humans also have the experimental confound of being outbred. Approaches in this case range from the use of twin studies to family-based analyses (34). In systems where controlled crosses can be carried out, a wider range of options are possible (2, 35, 12, 13). These approaches have been particularly effective in breeding

23

programs, where intragenotypic variability is not desirable (2). In fact the idea that there may be genetic variation underlying phenotypic variability dates back to the 50's (36, 37, 38), but the actual estimates of the heritability of this component are more recent and primarily derived from outbred organisms, using family-based analyses in agricultural species ranging from rabbits to dairy cows (reviewed in 2). By using a model organism to study the mechanisms underlying variability, our study adds to a growing body of literature recognizing the importance of variance control in complex trait genetics.

Materials and Methods:

Drosophila stocks: The DGRP consists of a collection of isofemale lines derived from a single field collection from the Raleigh NC farmers' market, followed by 20 generations of full-sib mating that rendered most loci homozygous within lines (expected F = 0.986 (19)). The DGRP lines are available from the Drosophila Stock Center (http://flystocks.bio.indiana.edu). Stock used for Ten-a validation: Berlin-K, central-body-defectKS96, Df1-Ten-a, and RNAi TRiP.JF03375 (tub-Gal4;tub-Gal80ts > UAS-TRiP.JF03375). All flies were reared on standard fly media (Scientiis and Harvard University BioLabs fly food facility), in a single 25°C incubator at 30-40% relative humidity with a 12/12h light/dark cycle. Before each assay flies were fully randomized across: blocks, lines, Y-maze arrays and position on the array. At least 3 strains were assayed simultaneously on each array.

Phenotypic assay: Each experiment examines one array of 120 Y-mazes (refered to as maze-array). Mazes were illuminated from below with white LEDs, imaged with 2MP digital cameras, and the X-Y positions of each fly centroid was automatically tracked and recorded with custom written software. Further details about the assay are provided in (18), code available at http://lab.debivort.org/neuronal-control-of-locomotor-handedness/. We estimated the degree of variability of each line, using the Median Absolute Deviation (MAD) (4, 13). It is defined as the median of the absolute deviation from each observation's median: MAD = median (|X_i –

median(Xi)|). Where Xi is the phenotypic score of an individual fly within a line. MAD scores were computed for each line for each phenotype. Only females were used in this experiment and only lines yielding data from a minimum of 75 individuals were included. Fly behavior in the mazes was monitored for 2 hours. This assay generated four phenotypes: (A) The handedness or left/right turning bias in the arms of the maze summed over all L/R decisions. (B) The number of turns over the 2 hour period, an estimate of overall locomotor activity. (C) The "switchiness" of the right/left turn sequence, which is related to the mutual information between successive turns, (e.g. LLLLLRRRRR: low switchiness, high mutual information; LLRLLRRRLR: moderate switchiness, low mutual information; LRLRLRLRLR: high switchiness, high mutual information) defined as: $(N\langle L,R\rangle+N\langle R,L\rangle)/(2NRNL/N)$, where $N\langle L,R\rangle$ is the number of left turns followed by right turns, $N\langle R,L\rangle$ is the number of right turns followed by left turns NR is the number of right turns, NL is the number of left turns, and N is the total number of turns. (D) The regularity of turn timing: a fly with a high score makes turns uniformly throughout the experiment while a low score would characterize a fly making a small number of dense streaks of turns but is inactive for dozens of minutes at a time. It is defined as MAD(ITIs)/(7200/N) where ITIs is the vector of inter-turn intervals in seconds.

Quantitative genetic analysis:

Analysis of Means: In order to determine if there was genetic variation segregating in the DGRP affecting the mean turning bias, we partitioned the variance for line means using the ANOVA model: Y = μ + Lrandom+ Brandom + L*B random + A + X + A*X + e where Y is turning bias score of each fly, L is the effect of line treated as random, B is the effect of block treated as random, X the box effect, A the maze-array effect and e is the error variance (Extended Data Table 1). ANOVA implemented using PROC MIXED in SAS 9.3. Variance heterogeneity: We used several statistical approaches to estimate heterogeneity of variance for turning bias between lines (Extended Data Table 1). (A) The Brown-Forsythe test which is based on a one way ANOVA and relies on the absolute deviation from the median (4, 45). (B) Non parametric

bootstrapping in which we first pooled all the turn bias scores for all individual flies across lines, then resampled each line experimental group from this pool, matching the sample size. Lines in which the MAD of the resampled group was closer to the MAD of the pooled data, in fewer than 10 of 10,000 resamples, were taken as significant. This tests the null hypothesis that each group is drawn from an identical distribution of observations, using MAD as a test statistic. (C) A nonparametric version of the Analysis of Mean for Variances (ANOMV) (46). This approach compares the group means of the Median absolute deviation MAD to the overall mean MAD under the null hypothesis that the group MAD means equal each line specific MAD (results in table S1), implemented in SAS 9.3 (). (D) Finally we used the same ANOVA model described above for the analysis of means but used the absolute deviation from the median (4, 5) as a measure for each fly as the dependent variable. This test was implemented using PROC MIXED in SAS 9.3. Phenotypic correlation between traits: We assesed 4 traits as measured in our study and 4 additional traits gathered from the literature (standard deviation for starvation, startle response, chillcoma recovery, coefficient of environmental variation for night sleep). Data from (19) and (20). Phenotypic correlation between each trait pair was computed as the Pearson product-moment correlation. P-values were not corrected for multiple comparison. Implemented using PROC GLM in SAS 9.3.

High and low variance lines intercrosses: In order to confirm that variability was heritable, we crossed high variability lines 45 and 105 together, and low variability lines 796 and 535 together. We assessed statistical significance between parental lines and their progeny using the Brown-Forsythe test and a bootstrapping 2-tailed z-test (with n = 10,000 resamples). We resampled the turn bias of the parents and for each iteration calculated the MAD of turning bias then compared the MAD for the F1 progeny to their parents.

Genome wide association mapping:

GWAS was performed using the code and approach decribed in (19) (http://

dgrp2.gnets.ncsu.edu). We fitted a series of loci specific mixed linear model using the model: Y

= μ + Sb + Iu + e Where Y is the MAD of turning bias of each DGRP lines, S is the design matrix

for the fixed SNP effect b, we is the incidence matrix for the random polygenic effect u, and e is

the residual (19). A total of 1,931,250 SNPs and indels were used in our analyses with the minor

alleles present in at least 7 DGRP lines, using only biallelic sites. For each tissue, we used

FlyAtlas AffyCalls (23) to determine which genes were expressed in which tissue. To determine

significance we used a Fisher exact test comparing the expected number of gene expressed in

each tissue across the entire genome to the observed number of gene expressed in each tissue

in our gene list.

Validation of Ten-a effect on variability: Ten-a null and deficency: The turning bias and MAD

of turning bias of homozygotes of both the null allele Ten-acbd-KS96(26) and deficiency

overlapping Ten-a Df(1)Ten-a (27) were compared to heterozygous animals over their genetic

background, Berlin-K. Time course knockdown of Ten-a RNAi: 10 adult Ptub-Gal80ts;Ptub-Gal4/

Sb females were crossed to 3 UAS-Ten-a RNAi y1,v1;P(TRiP.JF03375)attP2 males for RNAi

induction. Flies were allowed to mate for 24 hours at 20°C at which point the parents were

removed and the bottles containing F1 eggs were returned to 20°C until the beginning of their

heat shock window. Flies were exposed for 72 hours to 30°C temperature, in a sliding window

each day over 14 windows (Fig 3a). All flies assayed were between 3 and 5 days post-eclosion.

In parallel, each day developing flies of the same genotype were examined and counted to

determine the fraction of flies in each developmental stage at the time of RNAi induction (Fig

3b). Controls were performed using Ptub-Gal80ts;Ptub-Gal4/Sb females crossed to Canton-S

males and Canton-S females crossed to UAS-Ten-a RNAi y1,v1;P(TRiP.JF03375)attP2 males

(Fig 3d), otherwise treated identically. Ten-a expression: Data for Ten-a expression over

developmental time (Fig 3c) were downloaded from FlyBase and derived from ModEncode

(modENCODE DDC ids: modENCODE_4433, _4435 and _4439 through _4462). This data

reflects animals synchronized by developmental stage to within 2h. To make this data

comparable to our experimental groups, in which egg-laying occurred over 24h, we

corresponded the developmental stages of the FlyBase data to our developmental stage time

course (Fig 3b), linearly interpolated the expression values and applied a 24h sliding window

average to the interpolated data, mimicking the dispersion effects of our longer egg-collection

window.

References

Mackay TFC et al. (2012) The Drosophila melanogaster Genetic Reference Panel. Nature
        482:173–178.

Buchanan SM, Kain JS, & de Bivort BL (2015) Neuronal control of locomotor handedness in
Drosophila. (under review at the time of submission)

Cheng X, et al. (2013) Ten-a Affects the Fusion of Central Complex Primordia in *Drosophila*.
PLoS ONE 8, e57129.

Young JM, & Armstrong JD (2010) Building the central complex in *Drosophila*: the generation
and development of distinct neural subsets. J Comp Neur 518:1525-41.

Shen X, Pettersson M, Rönnegård L, & Carlborg Ö (2012) Inheritance Beyond Plain Heritability:
Variance-Controlling Genes in *Arabidopsis thaliana*. PLoS Genet 8, e1002839.

Dworkin we (2005) A study of canalization and developmental stability in the sternopleural
bristle system of *Drosophila melanogaster*. Evolution 59:1500–1509.

Rönnegård L, & Valdar W (2012) Recent developments in statistical methods for detecting genetic loci affecting phenotypic variability. BMC Genet 13:63.

Huang W, *et al* Natural variation in genome architecture among 205 *Drosophila melanogaster* Genetic Reference Panel lines. *Genome Res* 24:113–1208 (2014).

Harbison ST, McCoy LJ, & Mackay TF (2013) Genome-wide association study of sleep in *Drosophila melanogaster*. BMC Genomics 14:281.

Turner TL, & Miller PM (2012) Investigating natural variation in *Drosophila* courtship song by the evolve and resequence approach. Genetics 191:633–642.

Robinson SW, Herzyk P, Dow JAT, & Leader DP (2013) FlyAtlas: database of gene expression in the tissues of *Drosophila melanogaster*. Nucl Acids Res 41:744–750.

Brown MB, & Forsythe AB (1974) Robust Tests for the Equality of Variances. J Am Stat Assoc 69:364–367.

Nelson PR, Wludyka PS, & Copeland K (2005) The analysis of means: a graphical method for comparing means, rates, and proportions. SIAM.

Wagner G, & Altenberg L (1996) Complex adaptations and the evolution of evolvability. Evolution 50:967-976.

Wludyka PS (1999) Two non-parametric, analysis-of-means-type tests for homogeneity of variances. J App Stat 26:243–256.

Chintapalli VR, Wang J, Herzyk P, Davies SA, & Dow JA (2013) Data-mining the FlyAtlas online resource to identify core functional motifs across transporting epithelia. BMC Genomics 14:518.

Gelbart WM, & Emmert DB (2013) FlyBase high throughput expression pattern data.

modENCODE Consortium (2010) Identification of functional elements and regulatory circuits by Drosophila modENCODE. Science 330:1787-1797.

Littell, R. C. (2006). SAS for mixed models. SAS institute.

Page was left intentionally blank

Chapter II: Ring attractor dynamics emerge from a spiking model of the entire protocerebral bridge

Abstract

Animal navigation is accomplished by a combination of landmark-following and dead reckoning based on estimates of self motion. Both of these approaches require the encoding of heading information, which can be represented as an allocentric or egocentric azimuthal angle. Recently, Ca^{2+} correlates of landmark position and heading direction, in egocentric coordinates, were observed in the ellipsoid body (EB), a ring-shaped processing unit in the fly central complex (Seelig and Jayaraman, 2015). These correlates displayed key dynamics of so-called ring attractors, namely: 1) responsiveness to the position of external stimuli, 2) persistence in the absence of external stimuli, 3) locking onto a single external stimulus when presented with two competitors, 4) stochastically switching between competitors with low probability, and 5) sliding or jumping between positions when an external stimulus moves. We hypothesized that ring attractor-like activity in the EB arises from reciprocal neuronal connections to a related structure, the protocerebral bridge (PB). Using recent light-microscopy resolution catalogues of neuronal cell types in the PB (Wolff et al., 2015; Lin et al., 2013), we determined a connectivity matrix for the PB-EB circuit. When activity in this network was simulated using a leaky-integrate-and-fire model, we observed patterns of activity that closely resemble the reported Ca^{2+} phenomena. All qualitative ring attractor behaviors were recapitulated in our model, allowing us to predict failure modes of the putative PB-EB ring attractor and the circuit dynamics phenotypes of thermogenetic or optogenetic manipulations. Ring attractor dynamics emerged under a wide variety of parameter configurations, even including non-spiking leaky-integrator implementations. This suggests that the ring-attractor computation is a robust output of this

circuit, apparently arising from its high-level network properties (topological configuration, local excitation and long-range inhibition) rather than fine-scale biological detail.

Introduction

An animal navigating in its environment relies on landmarks to estimate its orientation and position (Collett and Graham, 2004). However, in the absence of visual cues, many animals maintain a representation of their heading and position without landmarks by continuously tracking their own motion to calculate navigation vectors to return to specific location, a process called path integration (Etienne and Jeffery, 2004). Numerous studies have identified patterns of neural activity that could represent heading, one of the elements needed for path integration. These studies have further shown that heading representations are tuned by visual information but can be updated in the dark, without any visual feedback (Taube, 2007; Varga and Ritzmann, 2016; Seelig and Jayaraman, 2015), presumably by exploiting self-generated motion cues like efference copy (Kim et al., 2015). By integrating heading and distance traveled, an animal can estimate its current position (McNaughton et al., 2007) and calculate a return vector. Heading estimation requires the tracking of variables in angular coordinates, a computation that can be accomplished by "ring attractor networks" (Solovyeva et al., 2016; Skaggs et al., 1995; Zhang, 1996).

In theoretical models of ring attractor networks, neighboring nodes connect to form a topological ring. The value of an angular variable is encoded in the radial position of a "bump" of neural activity within this ring. This bump arises through the combined dynamics of short range excitation and global or long range inhibition between nodes (Knierim and Zhang, 2012; Skaggs et al., 1995; Zhang, 1996). Asymmetric excitation of adjacent nodes causes the bump to move in the direction of the excitation as its previous position is inhibited. Importantly, these
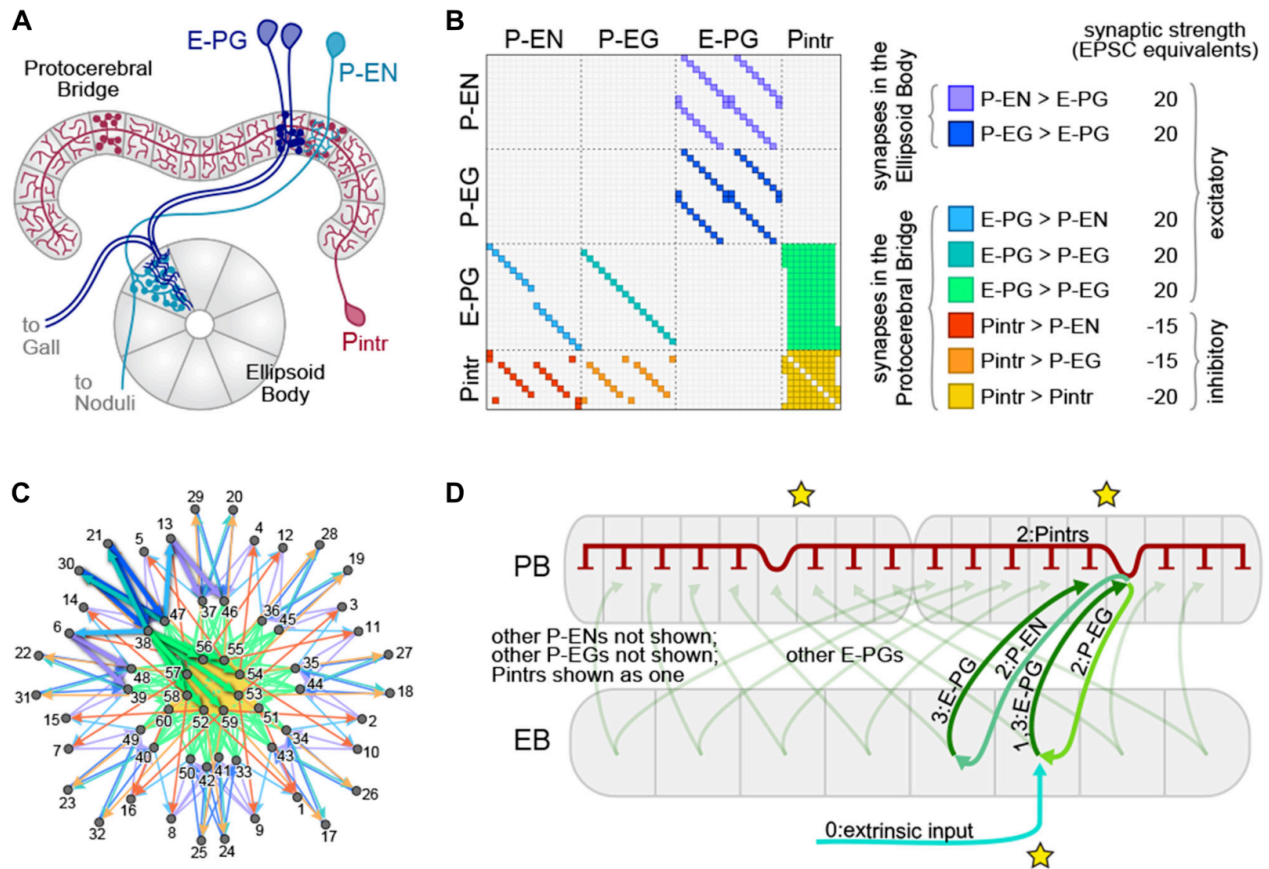
Figure 1 – *The Protocerebral Bridge neural circuit* – **A**) Diagram of the PB and EB, illustrating three out of four modeled neural subtypes, the E-PGs, P-ENs and Pintrs. Not shown are the P-EGs which project from the PB to the EB. Axonal arbors are indicated with circular varicosities/boutons. Dendritic arbors are intricate with fine linear branches. Overlap of an axonal arbor and a dendritic arbor within a single anatomical compartment (grey regions) is sufficient to postulate a synapse between neurons. Neurons with identical morphologies at the level of these anatomical compartments (e.g. the two dark blue E-PGs) are represented in the model as a single neuron. **B**) Matrix representation of the connectivity of the PB-EB circuit. A filled rectangle in row *i*, column *j* indicates a synapse, with neuron we presynaptic, and neuron *j* postsynaptic. Different fill colors indicate different synapse classes, whose within-class strengths are drawn from a single distribution. In most implementations, the distributions of synapse strength associate with synapse classes have 0 variance, and means as shown at right. **C**) Graph, with node positions determined by a force-directed algorithm of the network with connectivity shown in B), which forms a ring with bilateral symmetry. Thick edges indicate lateral and reciprocal excitatory loops (local excitation) from neuron 38 (as an example) as well as excitatory connections to inhibitory neurons that target all glomeruli (long-range inhibition). **D**) Schematic of key circuit motifs in the PB-EB network. Green and blue arrow represent excitatory neurons, red arrows inhibitory neurons. All E-PGs are shown to illustrate the mapping of the EB to each PB hemisphere. Only one P-EG and one P-EN are shown. The pool of Pintrs are represented as a single neuron. Stars indicate the position where the bump will emerge in the EB and the PB hemispheres. Numbers on labels indicate the sequence in which neurons are activated.

33

neighboring nodes do not have to be physically adjacent but adjacent only in connectivity. In mammals, ring attractors are thought to explain the dynamics of the head direction (HD) cells, which are primarily found in the thalamus and cortical areas associated with the hippocampus (Taube, 2007). Each HD cell is tuned to a particular head orientation in the horizontal plane and the direction in which the cell fires maximally is referred to as its preferred direction. Activity in topologically neighboring HD cells encodes continuously varying allocentric directions and the motion of the bump through the functionally (though not physically) ring-shaped network of HD cells encodes head orientation. Studying dynamics in mammalian neurons encoding head direction is difficult as they are spread across relatively large areas in of the brain and not spatially organized according to their preferred directions, making simultaneous monitoring of their activity challenging.

In insects, it was recently shown that a physically ring-shaped concentration of neuronal connections (neuropil) may function as a ring attractor (Seelig and Jayaraman, 2015) within the midline-spanning central complex (CX), of *Drosophila melanogaster*. Specifically, the ellipsoid body and protocerebral bridge may contain a neural circuit implementing a ring attractor. The EB neuropil has a closed ring shape in dipteran insects but is split ventrally and therefore roughly linear or bean-shaped in all other insect groups, where it is called the lower division of the central body (Strausfeld, 1976). Due to the evolutionary conservation of morphological cell types in the CX, it likely retains ring-shaped functional connections in all insects (Pfeiffer and Homberg, 2014). Furthermore, the lower division of the central body has been shown to encode the angular position of the sun in locusts, a continuous variable in angular coordinates, suggesting ring-like function without closed ring shape (Heinze, 2014; Homberg et al., 2011; Heinze and Homberg, 2007). In dipterans, the compact size and physical ring shape of this neuropil uniquely facilitates the study of putative ring attractor dynamics in an complete and

intact circuit that can be simultaneously imaged in an awake behaving fly (Seelig and Jayaraman, 2015).

In a closed-loop behavioral setup, Ca^{2+} activity in putative dendritic processes of one neuronal population within the EB was shown to encode relative angular position of a vertical stripe on a 2-D light emitting diode screen (Seelig and Jayaraman, 2015). Seelig and Jayaraman noted several features of their circuit that are typical of ring attractor networks (Haferlach et al., 2007; Knierim and Zhang, 2012; Arena et al., 2013). The Ca^{2+} activity in the so-called "wedge neurons" was localized in a single bump at any one time and this bump moved in response to the animal changing its heading. Furthermore, the bump exhibited spatial stability. When the fly was stationary for a long period of time, the bump would sometimes fade, but it typically reappeared in the same location when the fly resumed moving. This suggests the bump can be stored in ways other than than Ca^{2+} concentration, such as subthreshold voltages. The bump locked onto a single stripe when two competitor stripes were presented and was observed to jump between identical stripes from time to time. While these bump dynamics were recorded in the context of a closed-loop behavioral assay, causal relationships between the bump, behavior, motor commands and efference copy signals have not yet been identified.

The neurons exhibiting these ring attractor-like dynamics connect two of the neuropil that make up the CX, tiling the EB with dendritic arbors and the PB with presynaptic boutons (Figure 1). They are called E-PGs (Ellipsoid Body-Protocerebral Bridge-Gall neurons, called PBG1–8.b-EBw.s-D/Vgall.b in Wolff et al (Wolff et al., 2015), EB.w.s or "wedge neurons" in Seelig and Jayaraman (Seelig and Jayaraman, 2015) and EIP in Lin et al (Lin et al., 2013); see Table 1 for all abbreviations), denoting the flow of information within them from the EB to the PB and Gall (a secondary structure immediately outside the CX). The EB and PB are notable for their division into columnar segments, known as glomeruli in the PB and wedges/tiles (Wolff et al., 2015) in the EB. These neuropil contain many different neural cell types beyond those shown by Seelig

and Jayaraman to encode angular position. In the PB, these have been recently characterized at the level of morphology using single-cell stochastic labeling methods (Lin et al., 2013; Wolff et al., 2015). The resulting catalogue revealed that of the approximately 18 classes of neurons within the PB, only three reciprocally connected the EB and the PB.

We sought to test the hypothesis that PB neurons have circuit dynamics consistent with a ring attractor, using their connectivity as enumerated in these recent mapping papers. With a leaky integrate-and-fire model and simple connectivity rules, derived from light-microscopy resolution neuronal morphologies, we have found that a simple model recapitulates the bump of Ca^{2+} activity and essentially all of the *in vivo* dynamics previously observed (Seelig and Jayaraman, 2015). Furthermore, we have found that this circuit is robust to variation in synaptic weights, behaving like a ring attractor under a wide variety of parameters, perhaps indicating that computing a ring attractor is the primary evolutionary function of the reciprocal connection between the EB and PB.

Methods

Simulations were run in MATLAB 2015a and 2016a (The Mathworks, Natick MA USA) using custom scripts. All code to recapitulate these results is available at: *http://lab.debivort.org/ protocerebral-bridge-ring-attractor-model*

Network construction

To construct a circuit model of the PB we began with the catalogue of morphologically defined cell types in the PB (Wolff et al., 2015). This work enumerates all neuronal cell types within the PB, characterizing two cells as belonging to the same type if their pre- and postsynaptic arbors (as determined by MultiColor FlipOut imaging (Nern et al., 2015)) are in the same neuropil

36

compartments. Compartments are defined as spatially distinct regions of the major glia-ensheathed neuropils of the central complex and associated regions. For example, the PB itself contains 18 glomerular compartments and the EB contains 16 wedge and 8 tile compartments. We included in our model 1) any neuron with postsynaptic processes in the PB and presynaptic processes in other compartments (output neurons), provided there is a PB input neuron with a postsynaptic arbor overlapping the presynaptic arbor of that output neuron, and 2) any neuron with presynaptic processes in the PB and postsynaptic arbors that overlap presynaptic arbors of neurons projecting out of the PB (input neurons; Figure 1). This includes all the neuronal cell types catalogued in Wolff et al (2015) except for 5 classes of fan-shaped body projecting neurons (output only) and two classes of PB input neurons from the posterior slope (input only). We assumed that all neurons could be cleanly divided into dendritic and axonal compartments, and that information flows exclusively from the former to the latter.

The broad classes of neurons that met this criterion were the P-ENs (PB output neurons with axons in the EB and paired noduli), P-EGs (PB output neurons projecting to the EB and Gall), E-PGs (PB input neurons with dendrites in the EB and output to the Gall), and Pintrs (PB intrinsic neurons with both dendritic arbors and presynaptic boutons in the PB). See Table 1 for abbreviations. P-ENs and P-EGs comprise 16 types each, defined by which PB glomerulus contains their dendrites. E-PGs comprise 18 types, defined by which PB glomerulus contains their axons (unlike "wedge" neurons (Seelig and Jayaraman, 2015) E-PGs also include neurons innervating the first and last glomeruli of the PB G9L and G9R (Wolff et al., 2015)). The Pintrs comprise 10 types, defined by which PB glomerulus contains their axons. If their projections were identical at the level of the 60 types described above, individual neurons were considered identical, and represented by a single neuron in the model. Lastly, we assumed that neurons formed no autapses. The connectivity of the network thus defined is shown in Figure 1B. We

examined the topological arrangement of this network by using a force-directed algorithm (Fruchterman et al., 1990; Webb and Stone pers. comm.) to arrange nodes representing neurons. The connectivity present in this network has a ring-like topology, with bilateral symmetry (Figure 1C). From this representation, key circuit motifs can be discerned (Figure 1D). Input depolarizing the E-PGs has the potential to 1) activate a excitatory E-PG / P-EG loop, 2) activate adjacent E-PGs via the P-ENs, and 3) broadly inhibit all PB glomeruli via the pool of Pintrs.

Circuit physiological assumptions

Circuit dynamics were implemented using leaky-integrate-and-fire (Stein, 1967) neuronal models, with values for the membrane capacitance, resistance, resting potential, undershoot potential, and postsynaptic current (PSCs) time constants and magnitudes, chosen to reflect generic neuronal properties (Hodgkin and Huxley, 1952). The important free parameters of the model were the strengths and signs of the synapses between each type of neuron. We assume that the strengths of all synapses between two classes of neurons (a "synapse class;" e.g. all synapses between P-ENs and E-PGs) were identical.

Strength of synapses was implemented as the number of PSC equivalents per action potential. Excitatory neurons induced positive, depolarizing currents in their postsynaptic partners and inhibitory neurons negative currents. We assumed all neurons were excitatory unless we had evidence otherwise. The Pintrs are glutamatergic (Gelfand et al., 2008) and possess connectivity similar to other inhibitory local neurons in spatially compartmentalized neuropils, e.g., the antennal lobe (Chou et al., 2010) and lateral horn (Fişek and Wilson, 2014), therefore we assumed they are inhibitory (Liu and Wilson, 2013).

To deliver inputs to the circuit, we assumed that information first flows into the EB (this assumption has no bearing on our qualitative conclusions). Therefore, for each run of the model, the timing of action potentials in not-explicitly-simulated neurons upstream of the E-PGs was determined. These action potentials induced in the EBs excitatory currents with a strength equivalent of one PSC each. We assumed that background activity in these upstream neurons produced a Poisson-process sequence of action potentials with a mean rate of 5Hz. On top of this, Poisson-process spikes at higher rates (peaking at 120Hz) in subsets of E-PG types represented sensory-like input into the PB (Figure 2A), e.g. the azimuthal angle of light polarization (Heinze, 2014; Bockhorst and Homberg, 2015) or the retinotopic position of a landmark (Seelig and Jayaraman, 2013; Seelig and Jayaraman, 2015).

Circuit simulations

The circuit network structure was coded from the morphology descriptions in Wolff et al. (Wolff et al., 2015) per the rules described in the Results section below. Leaky-integrate-and-fire dynamics were used to simulate spiking neurons, and implemented using Euler's method to evaluate the following equation, with $\Delta t = 10^{-4}$s:

$$dV_i/dt = \frac{1}{C_m}(\frac{V_0 - V_i}{R_m} + I_{\text{in}} + \sum_{j=1}^{60} M_{j,i}I_j + I_{\text{ect}})$$

where V_i is the membrane voltage of neuron i, I_{in} is input current from neurons outside the PB-EB circuit (0 in all neurons other than the E-PGs), $M_{j,i}$ is the network connectivity matrix with entries equal to the synapse strength (in units of excitatory or inhibitory postsynaptic currents (PSCs)), I_j is the output current of other neurons in the PB-EB circuit, and I_{ect} is simulated ectopic current (such as might be induced by thermogenetic or optogenetic manipulation). We used parameter values that correspond to a generic spiking neuron (Hodgkin and Huxley, 1952), but these values are consistent with various *Drosophila* measurements or measurements of PB neurons in other species. C_m is the membrane capacitance (0.002µF in all neurons,

assuming a surface area of 10^{-3}cm^2; (Gouwens and Wilson, 2009)), V_0 is the resting potential

(-52mV in all neurons; c.f. (Rohrbough and Broadie, 2002; Sheeba et al., 2008)), R_m is the

membrane resistance (10MΩ in all neurons; (Gouwens and Wilson, 2009)), When a neuron's

voltage reached the firing threshold of -45mV (V_{thr}; c.f. (Gouwens and Wilson, 2009; Sheeba et

al., 2008)), a templated action potential trace was inserted into its voltage time series. This trace

was defined as follows:

$$
V(t) = \begin{cases} V_{\text{thr}} + (V_{\text{max}} - V_{\text{thr}})\dfrac{\text{Normpdf}(0,1,-1+\frac{t}{t_{\text{AP}}/2})-\alpha}{\beta} & : 0 < t < \frac{t_{\text{AP}}}{2} \\[2mm] V_{\text{min}} + (V_{\text{max}} - V_{\text{min}})\dfrac{\sin((t-\frac{t_{\text{AP}}}{2})\frac{2\pi}{t_{\text{AP}}}+\frac{\pi}{2})+\gamma}{\delta} & : \frac{t_{\text{AP}}}{2} < t < t_{\text{AP}} \end{cases}
$$

Where V_{max} is the (purely cosmetic, as it does not affect the circuit dynamics) peak action

potential voltage (20mV; c.f. (Rohrbough and Broadie 2002)), V_{min} is the spike undershoot

voltage (-72mV; c.f. (Nagel et al., 2015)), t_{AP} is the length of an action potential (2ms; c.f.

(Gaudry et al., 2013; Gouwens and Wilson, 2009)), Normpdf (a,b,c) is the probability density

function of a Gaussian with mean a, standard deviation b at c, and α, β, γ and δ are

normalization parameters so that the max and min of the Normpdf and sin segments are 1 and

0 respectively prior to scaling by the voltage terms.

The firing of an action potential also triggered the addition of a templated postsynaptic current

(PSC) trace to the output current time series of the firing neuron. The PSC trace was defined as

follows in terms of t in ms:

$$
I(t) = \begin{cases} I_{\text{PSC}}\dfrac{\sin(\frac{t\pi}{2}-\frac{\pi}{2})+\alpha'}{\beta'} & : 0 < t < 2 \\[2mm] I_{\text{PSC}}\dfrac{2^{-(t-2)/t_{\text{PSC}}}+\gamma'}{\delta'} & : 2 < t \leq 2 + 7t_{\text{PSC}} \end{cases}
$$

Where I_{PSC} is the amplitude of a PSC (5nA; c.f. (Gaudry et al., 2013); excitatory and inhibitory

PSCs were assumed to have the same magnitude but opposite sign), t_{PSC} is the half-life of PSC

decay (5ms; c.f. (Gaudry et al., 2013)), and α', β', γ' and δ' are normalization parameters so that

the max and min of the sin and exponential terms are 1 and 0 respectively prior to scaling by

I_{mini}. PSC traces had a length equal to $2+7t_{PSC}$ ms, corresponding to 2s of rise time plus 7 times the decay half-life.

Synapse strength parameters were explored manually to identify the baseline configuration in Figure 1. Thereafter parameter exploration was conducted as described in the Results. The overall magnitude of the synapse strength parameters shown in Figure 1 was the main free parameter of the model. The average synapse strengths of each synapse class are also free parameters, though we found that adjusting only the strengths of the Pintr>P-EG and Pintr>P-EN synapse classes was sufficient to recapitulate bump dynamics.

Leaky-integrator dynamics were used to simulate non-spiking graded potential neurons, and were implemented using Euler's method to evaluate the following equation, with $\Delta t = 10^{-4}$s:

$$dV_i/dt = \frac{1}{C_m}(\frac{V_0 - V_i}{R_m} + I_{in} + I_{max}\sum_{j=1}^{60} M_{j,i}\tanh(20*(V_j - V_0)))$$

Where all variables and constants are as defined above, and I_{max} is the maximum postsynaptic current achievable in a synapse of strength 1 within the PB-EB circuit. First, the scaling parameter of the current-voltage tanh transfer function (20) was determined empirically. This value yielded dynamics that were the most bump-like, given the synapse strength parameters determined in the leaky-integrate-and-fire model. Then, synapse strength parameters that produced a fully functional bump were identified by adding Gaussian noise to the baseline parameters from the leaky-integrate-and-fire model. This noise had mean of zero and a standard deviation of 100% of the baseline value of each synapse parameter. The dynamics of approximately 200 such random configurations were examined manually, and those producing the best bump-like behavior were then iteratively refined using them as a new baseline, and then adding Gaussian noise with a standard deviation of 10% and then 5% of the respective baseline values. The formula for these dithered synapse strength parameters was (s_k is the strength of synapse class k, s'_k is that parameter after dithering):
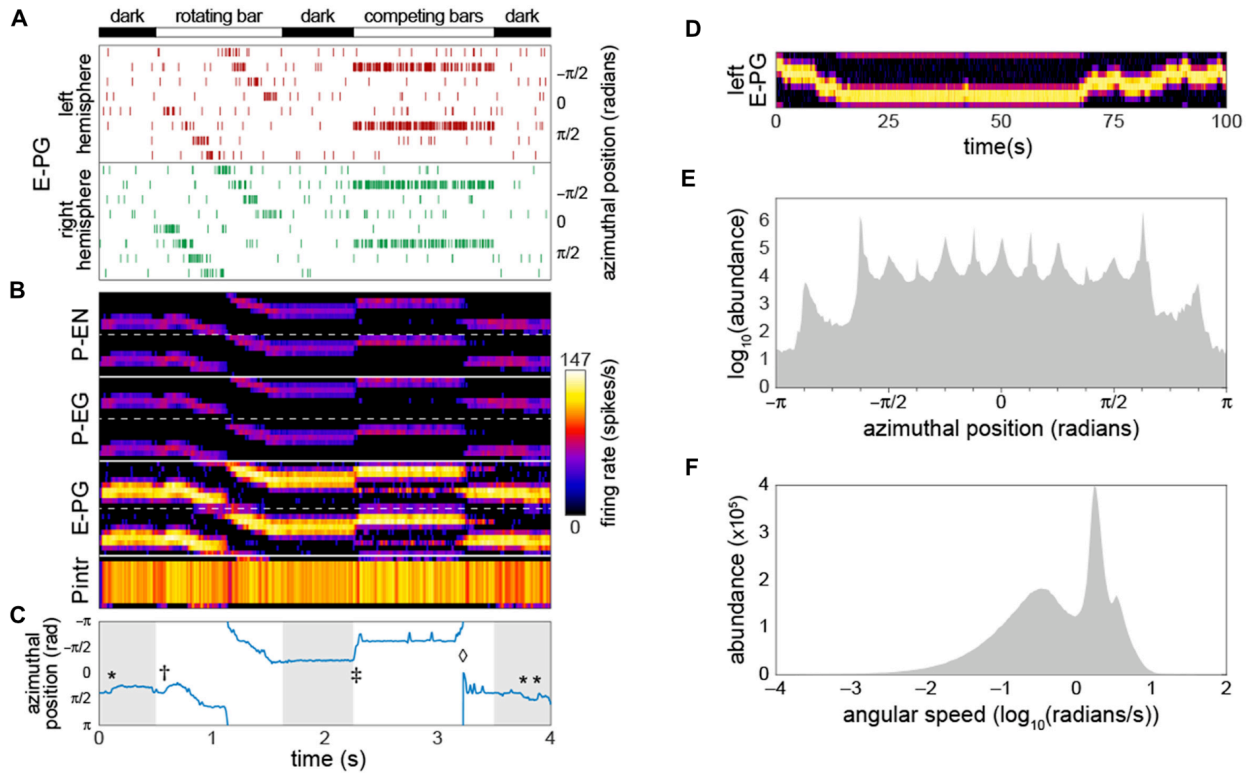
Figure 2 – *Bump-producing circuit dynamics* – **A**) Input into the circuit is delivered as action potentials (raster marks) in neurons upstream of the E-PGs, plotted vs. time. Various sensory stimuli can be represented, including rotating bars, and static competitors. In "dark" periods, the only input is Poisson-distributed background activity. Inputs are associated with the 8 tiles (Wolff et al., 2015) of the EB, and corresponding azimuthal angles in body coordinates are indicated. **B**) Activity of all 60 neurons in the circuit versus time. Plotted heatmap is a Gaussian-convolved raster of action potential times (standard deviation 24ms). Dotted lines demarcate left from right hemispheres within a neural subtype. **C**) Position of the bump (centroid of activity in B; blue line) versus time. * indicates "spontaneous" shifts in the position of the bump in darkness. † indicates the bump sliding to the position of a bar as soon as it appears, and then following it as it rotates. ‡ indicates the bump jumping to the position of a single competitor when two static competitors appear. ◊ indicates the bump spontaneously switching its position to that of the other competitor. **D**) Bump behavior in darkness vs time over a prolonged period in the left hemisphere E-PGs. **E**) Histogram of bump frame-by-frame centroid position over 383 simulations of four seconds each in darkness. **F**) Histogram of spontaneous bump motion speed in the same dark simulations.

$$s'_k = s_k(1 + \text{Norm}(0, \sigma))$$

In order to break initial symmetry and allow the bump to move "spontaneously" random Gaussian noise with mean zero and standard deviation of 3×10^{-10}V was added to each neuron in each timestep. Bump position was estimated and visualized by convolving the action potential rasters of each neuron with a Gaussian kernel with a standard deviation of 24ms. This approximates a Ca^{2+} signal in these neurons. Bump position was determined by taking the centroid, modulo eight, of this convolved representation for the P-ENs in each hemisphere. The estimated centroid of each hemisphere's P-ENs was averaged to produce the final centroid estimate.

Circuit dynamics parameter sensitivity analysis

Circuit dynamics were captured for multidimensional analysis by simulating the network for 2 seconds, with inputs representing a rotating bar and two static competitors (setting parameters *SweepBarBool* and *TwinBarBool* equal to one in PBexperiment.m). Starting from the baseline synapse strength parameters, we added Gaussian noise to each parameter using the dithering formula above. Circuit dynamics during the rotating bar and competitor bar stimuli are particularly diagnostic of bump performance. We trimmed the circuit "Ca^{2+} signal" time series to 200ms from each of these two stimulus periods, then subsampled the timepoints 20:1, yielding a final 200 diagnostic timepoints). Dynamics from 10,000 networks with randomly dithered synapse strength parameters were computed, each yielding a single point in a 12,000 dimensional space representing circuit dynamics (200 diagnostic time points x 60 neurons). In addition, we added points representing the dynamics of networks in which a single synapse class parameter value was swept systematically from -9x to 10x its original value. The dynamics from these systematic sweeps were added to the dynamics from the randomly dithered networks and projected into two dimensions using PCA for visualization. Clusters of dynamics

were enumerated using *k*-means clustering in the original 4,000 dimensional space. Representative dynamics of each cluster were computed by averaging all of the Gaussian-convolved spike rasters receiving each *k*-means cluster label.

Results

Bump circuit dynamics

As a starting point for our characterization of circuit dynamics, we assumed, rather arbitrarily, that all synapse classes had a strength of 20 PSCs. With a small amount of manual parameter searching, we found that if the inhibitory synapses between the Pintrs and the P-ENs and those between the Pintrs and P-EGs had strengths of 15, circuit activity recapitulated several key phenomena that have been observed in Ca^{2+} recordings of the E-PGs (Figure 2B,C; Movie 1): 1) a stable "bump" of activity appeared at one position in the glomerular axis of the PB and the corresponding EB position, as observed by Seelig and Jayaraman (2015). This bump was almost always distributed over two or three glomeruli/tiles (25% to 38% of the azimuthal axis), corresponding roughly to the size of the Ca^{2+} bump they imaged (Seelig and Jayaraman, 2015). 2) The bump jumped or slid to the position of a novel sensory cue (i.e. a vertical bar), represented as increased firing rate in the neurons upstream of a single E-PG. 3) When the position of this input activity moved across adjacent glomeruli (moved in its azimuthal position), the bump followed. 4) When two competing vertical bars were provided in the form of firing-rate-matched activity upstream of two non-adjacent E-PGs, the bump moved to the position of one of the cues. 5) Occasionally, during the presentation of competitor bars, the bump would switch positions from one cue to the other. These characteristics were present for a wide range of synapse strength parameters (see stability analysis below).

44
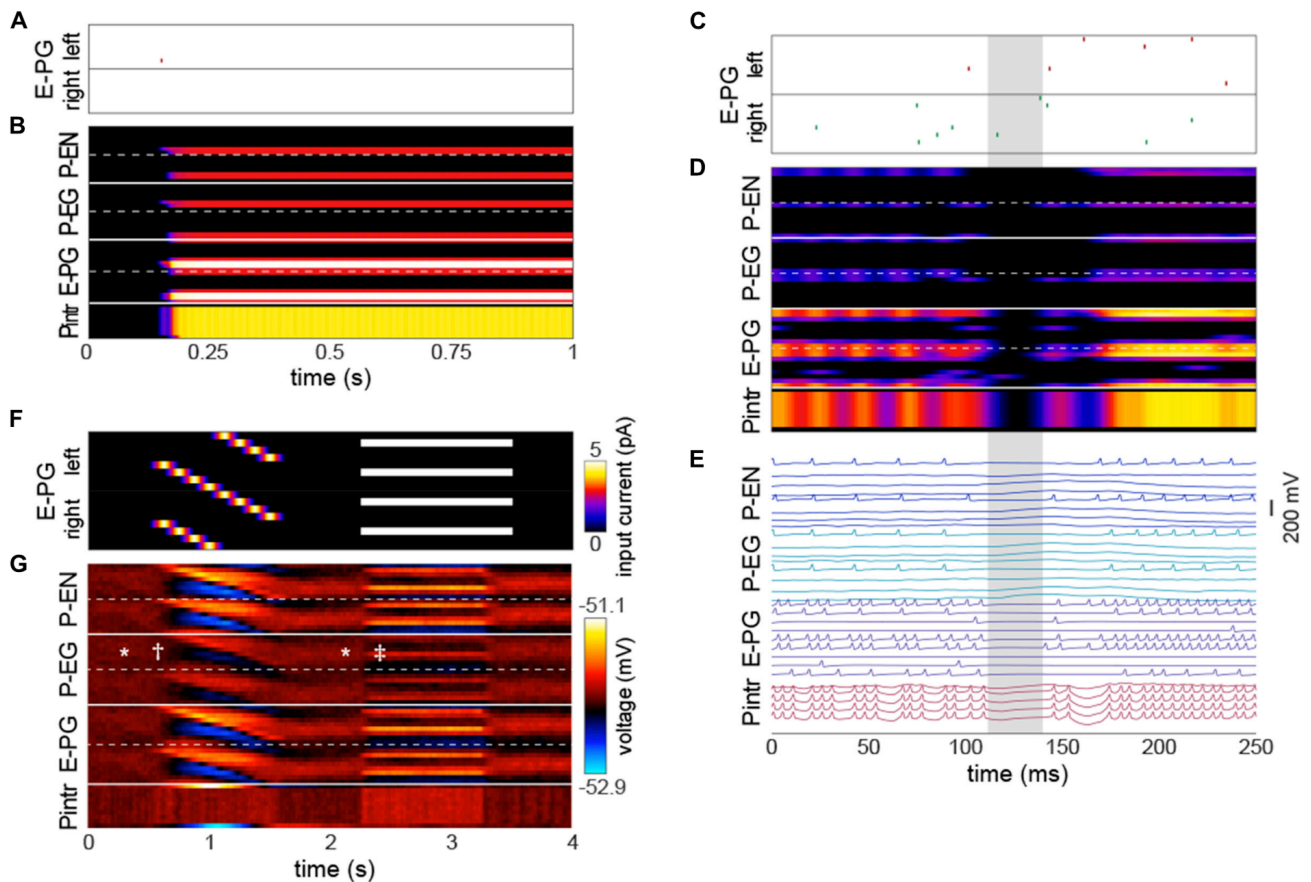
Figure 3 – *The bump requires action potentials, but can persist momentarily without them* – **A**, **B**) Input of a single action potential in an E-PG (red raster mark) is sufficient to induce a stable bump in the circuit. B) Gaussian-convolved raster of neural activity in all neural subtypes (axes and color scale as in Figure 2B). **C**) Circuit input via the E-PGs corresponding to 250ms of darkness. **D**) Corresponding dynamics of all neurons in the circuit revealing a ~20ms window (shaded grey) in which the bump disappears is not represented in action potentials, but reappears in the same position after the window (axes and color scale as in Figure 2B). **E**) Corresponding voltage traces. For clarity, the trace of every other neuron has been removed. **F**) Depolarizing currents representing input into the E-PGs in a leaky-integrator implementation of the circuit, versus time. Synapse strength parameters used were those that provided dynamics most closely approximating a bump. **G**) Corresponding voltages in the entirety of the circuit. Symbols indicate elements of canonical bump phenomenology, as in Figure 2C. * indicates "spontaneous" shifts in the position of the bump in darkness. † indicates the bump jumping to the position of a bar as soon as it appears, and then following it as it rotates. ‡ indicates the bump jumping to the favoring one of two competitors (the lower competitor, most clearly discernible in the left hemisphere — the top half of each neuron type).

As reported by Seelig and Jayaraman (2015), the bump appeared to be fairly stable in the dark (i.e. with only baseline background activity present upstream of the input neurons). Our baseline synapse strength parameter values yielded a bump "spontaneous drift rate" comparable to those observed *in vivo* (approximately 1 glomeruli/s; Figure 2D). We observed that the angular position encoded by the position of the bump had a highly discretized distribution while drifting in the dark (Figure 2E); the vast majority of the time, the bump was present in one of 15 azimuthal positions, and among these, $\pm 5\pi/8$ was the most abundant, followed by $\pm\pi/8$. The distribution of bump speed during spontaneous motion (i.e. any motion in the dark) was trimodal (Figure 2F). These modes may correspond to staying in position, sliding between adjacent positions, and jumping between non-adjacent positions.

Bump relation to action potentials

The emergence of a bump was remarkably robust, even a single action potential upstream of a single input E-PG was sufficient to induce a bump at the position of that action potential that would persist indefinitely in the absence of further action potentials (Figure 3A,B; Movie 1). We observed that occasionally the bump, as encoded by action potentials, would disappear briefly (up to a few tens of milliseconds at a time; Figure 3C-E). During these periods, none of the PB neurons would fire any action potentials, even if there were occasional action potentials in the neurons upstream of the E-PGs. This implies that the bump can be "stored" in sub-threshold potentials. These brief disappearances tended to happen when the bump was located at one of the less frequent azimuthal positions (e.g. $\pm 7\pi/8$).

Several sets of neurons appeared to fire synchronously in the circuit (Figure 3E), specifically, those Pintrs that have axonal arbors in two PB glomeruli, bilaterally paired P-ENs and P-EGs, and bilaterally paired E-PGs (though this group of neurons is somewhat less synchronous by

46
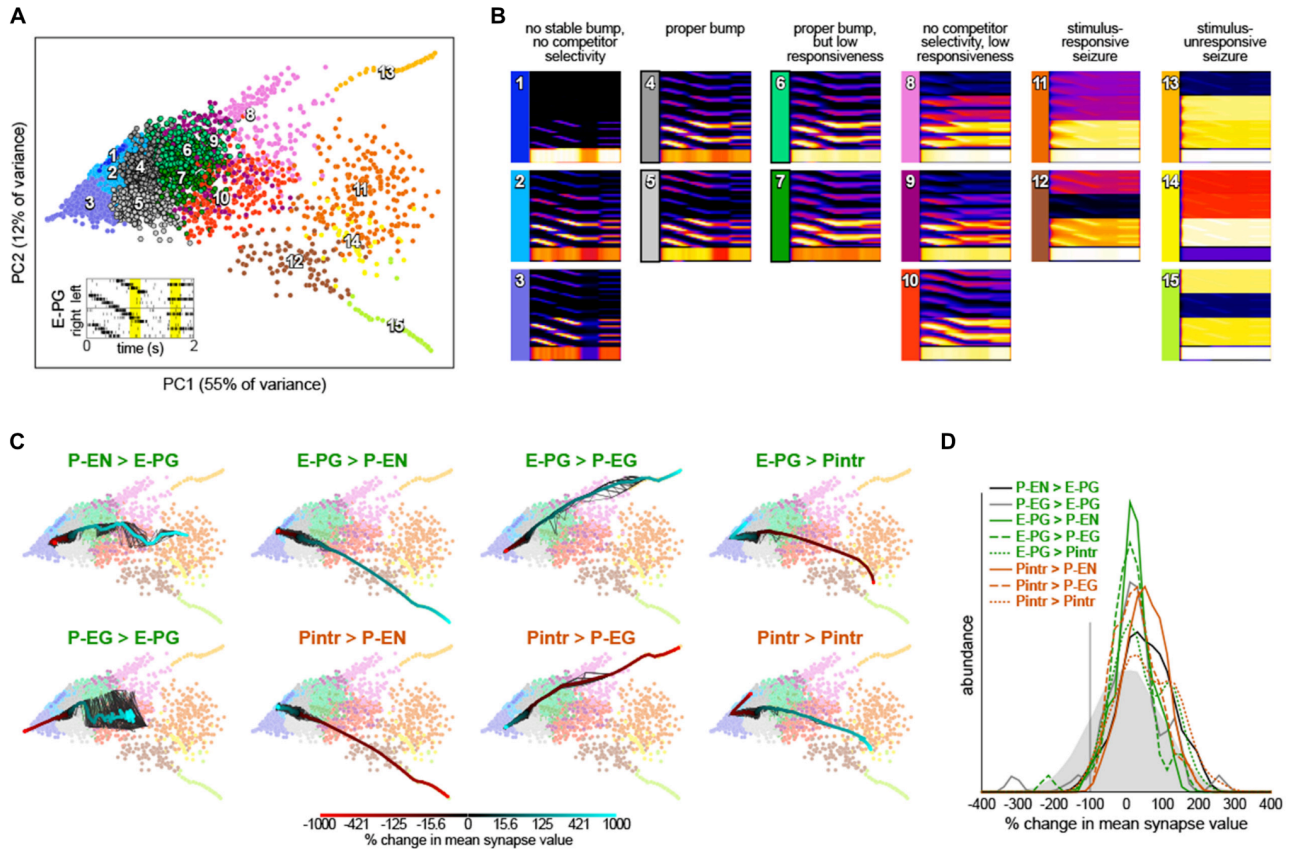
Figure 4 – *Robustness of bump dynamics* – **A**) Scatter plot of the first two principal components of circuit dynamics (during the yellow intervals of E-PG stimulation shown in the inset; see Methods). Each point represents the dynamics of a circuit with synapse strength parameters equal to either 1) the baseline parameters (Figure 1B) plus Gaussian noise with mean = 0 and standard deviation = 20% of baseline value, or 2) the baseline parameters, with one parameter varied adjusted by -9x to 10x of its baseline value. Colors indicate 15 *k*-means clusters computed prior to PCA. Numbers show the approximate cluster centers. **B**) Mean dynamics of all points within each cluster shown in A).. Each plot is an average of Gaussian-convolved action potentials rasters (as in Figure 2B). Numbers and colors correspond to those in A). **C**) Systematic variation of each of the eight synapse class strength parameter away from their respective baseline values. Black lines represent 10 different parameter value sweep replicates, and the thick color-mapped line their average, color coded by the shift of each respective parameter. **D**) Distributions of synapse parameters that support proper bump function. Gaussian noise from the solid grey distribution was sampled and added to each synapse class independently. This was repeated 24,000 times and the resulting circuit dynamics were k-means clustered into 400 clusters. 6 clusters were identified that had proper bump dynamics comparable to modes 4 and 5 of A). The distribution of offsets represented in these clusters is shown for each synapse class strength parameter.

virtue of their being the input neurons that are stimulated at random times by upstream neurons). Leaky-integrator implementations (without action potentials) of this model could also produce a bump that persisted in the absence of sensory input, selected between competitor bars or formed a unitary bump after competitors were removed (Figure 3F,G). However, the bump in this implementation did not have the same rapid spontaneous bump formation, spatial precision, or strong selectivity between competitors seen in the leaky-integrate-and-fire implementation (though it did have weak selectivity between competitors).

Synapse strength parameter sensitivity

We next examined whether we had serendipitously found the only synapse strength parameters that recapitulated so many experimental bump phenomena or were these dynamics robust to parameter values. We added random, Gaussian-distributed noise (mean = 0, standard deviation = 20% of each parameter's baseline value) to the synapse strength parameters and then stimulated these dithered circuits with inputs of 1) sequential bursts of activity in adjacent wedges representing a rotating bar and 2) elevated activity in two non-adjacent glomeruli representing stationary competitor bars (Figure 4A). For each of these configurations, the ensuing circuit activity in all neurons during diagnostic periods of this stimulation (200ms from the the rotating bar phase and 200ms from the beginning of the competitor bars) were treated as points in a high dimensional space of circuit behavior. These points were clustered and averaged within a cluster to provide an exhaustive catalogue of the modes of dynamics that this circuit topology can produce (Figure 4A,B). Of 15 modes, three feature sets of neurons with essentially no activity (modes 1-3) and five feature sets of seizing neurons (modes 11-15). Two of the remaining modes feature bumps exhibiting all the key properties observed experimentally (i.e. those shown in Figure 2): modes 4 and 5, which are distinguished largely by which competitor they select. Two modes have bumps that are stable on too-long timescales and

extend over too many adjacent glomeruli, but otherwise show the key properties (modes 6 and 7). The remaining three modes (8-10) have some key bump properties, but are stable on too-long timescales, are too wide, and fail to select between competitor bars. Thus, it appears that bumps with the properties observed by Seelig and Jayaraman are a robust output of circuits with this topology under a wide range of synapse strength parameters.

To understand the contribution of each synapse class to circuit function, we systematically varied the strength of each synapse class from -9x to 10x its original value (Figure 4C). Converting excitatory drive from the PB to the EB into inhibition (by reversing the sign of either the P-EN>E-PG or P-EG>E-PG synapses) eliminated input-independent bump activity in the P-EGs (mode 3). Increasing the strength of that excitatory drive led to too-stable bumps without competitor selectivity (modes 9 and 10) and eventually seizure across the circuit (mode 11). Increasing inhibition of P-ENs (by either reversing the excitatory E-PG>P-EN synapses or amplifying the strength of the inhibitory Pintr>P-EN synapses), not surprisingly, eliminated activity in the P-ENs (mode 1). Conversely, the opposite manipulations resulted in a too-stable bump (mode 10) and eventually seizure of the P-ENs (and E-PGs and Pintrs; modes 12 and 15). Increasing inhibition of P-EGs (by either reversing the excitatory E-PG>P-EG synapses or amplifying the strength of the inhibitory Pintr>P-EG synapses), not surprisingly, eliminated input-independent bump activity in the P-EGs (mode 3). Conversely, the opposite manipulations resulted in a too-stable bump (mode 8) and eventually seizure of the P-EGs (and E-PGs and Pintrs; mode 13). Increasing inhibition of Pintrs (by either reversing the excitatory E-PG>Pintr synapses or amplifying the strength of the inhibitory Pintr>Pintr), resulted in too-stable bumps (mode 7), bumps with no competitor selectivity (mode 10) and eventually seizure in P-ENs, P-EGs, and E-PGs (mode 14). The opposite manipulations eliminated input-independent bump activity in the P-ENs (mode 2) and eventually all activity in P-ENs and P-EGs (mode 1).
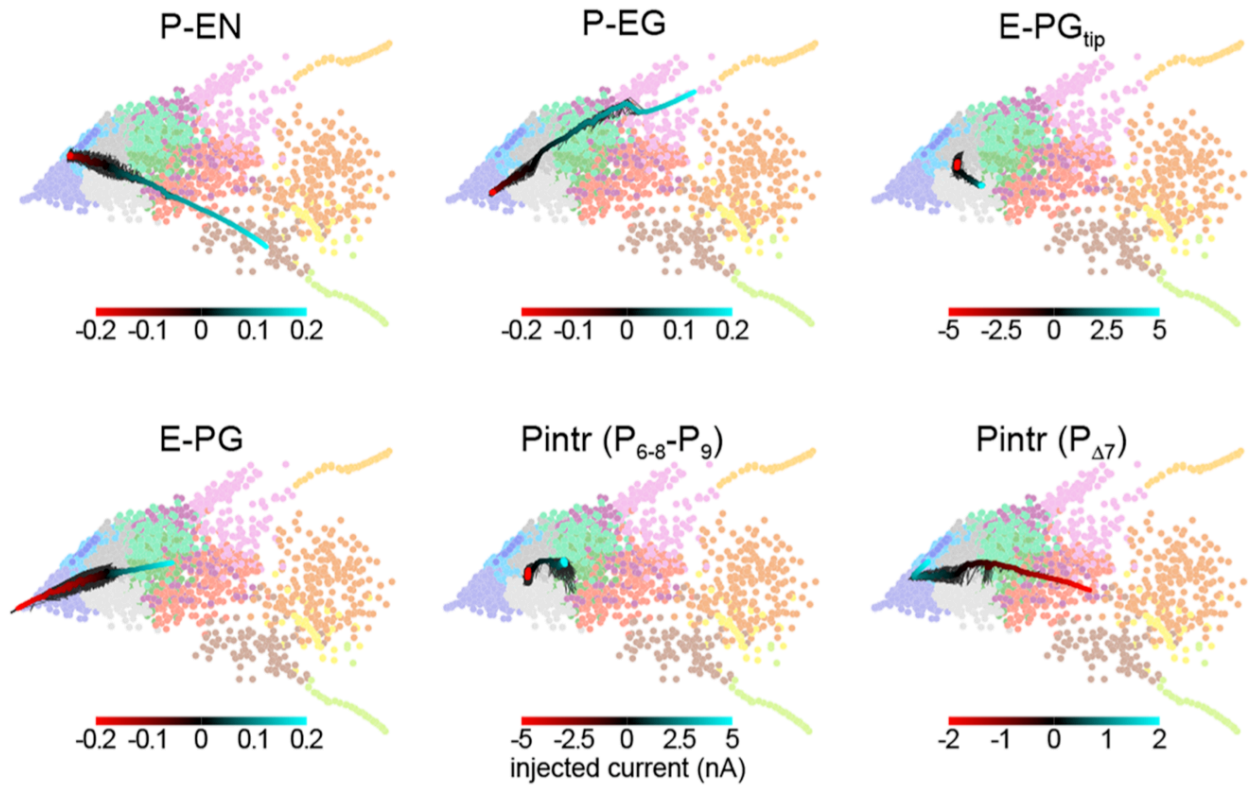
Figure 5 – *Prediction of circuit dynamics after physiological manipulation of neuronal subtypes* – Circuit dynamics projected into two dimensions using the same input stimulus, diagnostic intervals, subsampling and linear projection as Figure 4B. Labeled neuronal subtypes were "injected" with ectopic currents as might be brought about by thermogenetic or optogenetic manipulation. Black lines represent 10 different current sweep replicates, and the thick color-mapped line their average. E-PG$_{tip}$ refers to the subset of E-PGs that project to the Gall tip. Pintr(P$_{6-8}$-P$_9$) refers to intrinsic PB neurons that project from glomerulus 6-8 to glomerulus 9 and Pintr(P$_{\Delta 7}$) that tile the PB with boutons while projecting dendrites throughout the PB.

This systematic variation of synapse class strength parameter values also provides evidence of the robustness of the bump phenomenon in this circuit. Increasing or decreasing the strength of a synapse class by up to 50% of its baseline value, for example, seldom changes the mode of circuit dynamics (Figure 4C). Thus, it seems a sizable parameter subspace around the baseline

values can produce bump phenomena. This analysis allows us to assess how much of the parameter space around the baseline produces bumps, not how much of the total space can produce bumps. To discover more distant parameter configurations that might also work, we added a substantial amount of Gaussian noise to all parameters simultaneously (mean = 0, standard deviation = 100% of each parameter's baseline value; this reverses the sign of a parameter 16% of the time). The vast majority of circuits with these more broadly-sampled random parameter configurations seized or were silent in at least one neural subtype but a small portion (~1.5% of 24,000 random parameter configurations) exhibited correct bump phenomena. These were identified and pooled by *k*-means clustering of circuit dynamics.

The distributions of each parameter within this pool of bump producing circuits are shown in Figure 4D. Each parameter can evidently take on a wide range of values, and with the right corresponding changes in other parameters, support bump function. Notably, almost all parameters could even have their sign reversed from excitatory to inhibitory or vice versa, and still contribute to a bump-producing circuit. The exceptions were the Pintr>P-EN and Pintr>P-EG synapses, which could be silenced but not converted into excitatory synapses, and still produce a bump. In general, however, the random noise that was added to the parameters in bump-producing circuits was positive, meaning that excitatory synapses could generally be made more excitatory, and inhibitory synapses more inhibitory, without loss of bump function. Several parameter distributions appeared to be multimodal, notably P-EG>E-PG, E-PG>P-EG, E-PG>Pintr, and Pintr>Pintr, suggesting there may be discrete (or non-linear manifolds of) synapse strength configurations that support bumps.

Prediction of circuit manipulation effects

This framework allowed us to predict the effect of thermogenetic or optogenetic perturbation of neural populations. We computationally injected varying amounts of current into each neural subtype as defined by Wolff et al. (2015), i.e. distinguishing between E-PG and Pintr subtypes (Figure 5), and projected the ensuing circuit dynamics into the same space where we defined the dynamics modes (Figure 4B). In general the predicted effects matched the effects of changing the corresponding synapse class parameters. For example, injecting depolarizing current into the P-ENs had the same effect as increasing the strength of the excitatory E-PG>P-EN synapse class (or decreasing the strength of the inhibitory Pintr>P-EN synapse class). Injecting even relatively large (±5nA) currents into the gall-tip-projecting subset of E-PGs or the P_{6-8}-P_9 subset of Pintrs (Wolff et al., 2015) had little effect, presumably because these neural subtypes are less numerous in our model, represented by only 2 neurons each.

Discussion

Ring attractor networks are an appealing explanation for the storage and updating of continuous variables in the brain (Knierim and Zhang, 2012; Taube, 2007; Skaggs et al., 1995; Zhang, 1996) and may play a role in visual attention (de Bivort and van Swinderen, 2016). We have shown dynamics consistent with a ring attractor arise in a network of generic spiking neurons with connectivity inferred from light-resolution microscopy and few other assumptions. The neurons in this network represent classes of neurons that are morphologically identical down to the level of independent neuropil subcompartments (glomeruli/wedges) defined in recent efforts to catalogue all neurons in the protocerebral bridge of the central complex (Wolff et al., 2015).

The model produces a number of key behaviors that are predicted by ring attractor theory (Taube, 2007; Song and Wang, 2005) and observed by Seelig and Jayaraman (2015) by Ca^{2+}

activity in the E-PG neurons. In particular, a broad bump of activity (about 90-120° wide) tracks a simulated cue as it moves. When the cue is removed, the bump persists indefinitely, initially staying in the position of the now-missing cue. In the continued absence of external cues, the bump can "spontaneously" shift in position. These shifts are absent when there is no spike noise in the input neurons (Fig 3B). Thus, stochastic fluctuations in circuit input can move the bump, but it is hard to attribute these shifts to specific input spikes, perhaps not surprising considering the interconnected topology of the circuit.

We found that the bump may slide or jump to novel cues, and chooses only a single cue if multiple competitors are provided simultaneously (occasionally spontaneously jumping between them). Furthermore, we found that even when there is a pause in the representation of the bump by action potentials, it will reappear in the same position, as suggested by brief periods of time in which Seelig and Jayaraman (2015) observe the Ca^{2+} bump to disappear and reappear in the same position. These findings suggest the bump is stored in subthreshold voltages.

Interestingly, our model suggests that there are discrete positions in the network in which this bump of activity prefers to reside as it moves through the network. Whether this is true of the circuit *in vivo* is not yet known, but it has been reported that startled cockroaches turn and run at angles that are multimodally distributed (Domenici et al., 2008). The modes of these escape angles are separated by approximately 30°, which is nearly matched by the 13 modes of bump position that we observed (Figure 2E). Perhaps discretized bump position tendencies underlie this distribution of escape angles. The origin of these modes surely arises from the discrete segmentation of the PB into 9 glomeruli and the EB into 8 tiles/16 wedges. The modes appear to be evenly spaced every 22.5° between +/-112.5°. Outside that range, two modes appear at approximately +/-152°. The bump dwells in these modes one to two orders of magnitude less often than the other modes. Perhaps their spatial irregularity (compared to the other modes) is

related to their diminished stability. Furthermore, no mode is present at +/-180°, probably due to the broken radial symmetry of the circuit in this position (Figure 1C), which is associated with the PB being split into linear segments while the EB has circular topology. The distribution of bump speeds (Figure 2F) is also consistent with theoretical work predicting distinct modes of bump motion: sliding between adjacent positions and jumping between non-adjacent positions (Zhang, 1996). In general, sliding motion is induced when a stimulus moves slowly (or stochastic fluctuations increase near to the bump's current position. Conversely, the bump jumps when the stimulus moves rapidly (or stochastic fluctuations increase far from the bump's current position).

Additionally, angular position vectors can be coded not only by which neurons are active, but also by which pairs of neurons have synchronous activity (Ratté et al., 2013). In our circuit we found that neurons tended to fire synchronously (Figure 3E), indicating that perhaps the PB could conceivably participate participates in a synchrony-based code. However, the sets of neurons observed to fire synchronously, particularly the P-EGs and P-ENs (Figure 3A) are predicted by the number of monosynaptic connections each of these neuron classes is from the extrinsic inputs driving the circuit (Figure 1D). Thus, the synchrony in the system may be determined by its topology and not flexible enough to usefully code angular position.

By adding random noise to synapse classes, we determined that a large range of synaptic strength parameters can result in apparently proper ring attractor dynamics (Figure 4). Moderate levels of noise in the synaptic strengths within the circuit often still produced dynamics consistent with experimental observations. We were able to characterize potential failure modes of the network, which include absence of action potentials in classes of neurons, an inability to sustain the bump, low responsiveness, low or no competitor selectivity, and/or network seizures.

By systematically varying the values of synapse strength parameters one at a time, we explored the space of failure modes to evaluate the robustness of our model. Our model predicts that perturbing certain synaptic or neuronal classes could have larger impacts on this network than others. In general, neuronal classes with fewer neurons could be perturbed more dramatically before causing a breakdown in bump dynamics. At the same time, all the synaptic or neuronal classes could be dramatically perturbed (or even reversed in sign) and still produce a proper bump, provided appropriate compensatory changes in other classes were made. Going forward, our model may be able to provide a quantitative framework for understanding variability in individual differences in navigation, such as locomotor handedness, a behavior whose variability across individuals is controlled by neurons in the protocerebral bridge (Ayroles et al., 2015; Buchanan et al., 2015). Specifically, we can add noise to individual synapses, reflecting variation from developmental stochasticity and post-developmental plasticity (e.g., by analogy to our synapse class parameter dithering: $M'_{j,i} = M_{j,i}(1 + \mathrm{Norm}(0, \sigma))$).

It is important to consider which assumptions made in this model might not be realistic. The information flow of each neuron class is inferred from the overlap of "dendritic" and "axonal" cellular compartments determined by light-microscopy. Despite being unipolar, neurons in *Drosophila* generally have polarized information flow (Rolls, 2011), however, common axo-axonal, dendro-dendritic and perhaps even dendro-axonal synapses (Schneider-Mizell et al., 2016) paint a more complex picture. Electrical coupling, which can lead to synchronized neuronal firing, is also common in insect neurons (Pereda, 2014), but we have not included any in our model. Furthermore, we have assumed that every neuron has the same integration and firing dynamics despite the fact that the dynamics can vary significantly based on specific ion channel expression levels (Berger and Crook, 2015; Marder, 2011). We also make the assumption that if an axon and dendrite overlap in a compartment then they are connected, but

this is not necessarily the case. Neurons that are adjacent with the resolution provided by light microscopy may not come into physical contact (Feinberg et al., 2008). Moreover, axons and dendrites which are in contact do not necessarily form functional synapses (Kasthuri et al., 2015). Due to these caveats, it is remarkable that our model recapitulates so many of the experimental observations of Ca^{2+} of E-PG neurons.

The core computation of this circuit may be robust to many categories of biological detail, emerging instead from high-level connectivity of the sort that can be inferred from light microscopy. Indeed, leaky-integrator implementations of the model simulating graded neurons without action potentials produced passable bumps (Figure 3F,G). This suggests that bump dynamics are not only robust to synapse strength parameter variation, but also variation in neuron physiological parameters. However, the leaky-integrator implementation did not exhibit selectivity between competitor stimuli as sharp as the leaky-integrate-and-fire implementation. This suggests that spiking neurons are required to recapitulate experimental Ca^{2+} recordings, while not being required for bump dynamics in general.

Despite the conspicuous ring shape of the EB and its large number of inhibitory neurons with horizontal morphologies spanning all azimuthal positions (Martín-Peña et al., 2014; Kottler et al., unpublished), neither of these qualities is necessary to bring about ring attractor-like dynamics in our model. Instead, our model generates global inhibition using intrinsic PB neurons (the PBintrs; Figure 1). The EB has been shown to receive spatiotopic information about visual features from the bulbs (Seelig and Jayaraman, 2013) and is involved in visual place learning (Ofstad et al., 2011). These observations suggest that the EB encodes spatial information about landmarks in the environment which could be used to correct accumulated error in the position of a bump. While inhibitory circuitry within the EB is not required for ring attractor dynamics in the PB-EB circuit, we have no evidence that the inhibitory circuitry in the EB does not participate

in a ring attractor. It is possible that both the Pintrs in the PB and the ring neurons (Martín-Peña et al., 2014) of the EB implement long-range inhibition for the production of two distinct ring attractors, which could potentially interact to perform more sophisticated computations.

The egocentric heading correlate present in the PB-EB circuit is likely transmitted to other regions of the CX, particularly the fan-shaped body (FB). This neuropil could be a site of integration of navigational with internal state and sensory information for adaptive decision making. In addition to the PB-EB circuit neurons described here, the PB contains many columnar neurons projecting into the FB that have postsynaptic arbors in individual PB glomeruli and presynaptic boutons in different layers and columns of the FB (Wolff et al., 2015). Thus, it is likely that the FB inherits a bump or vertical band of activity from the PB. The FB is hypothesized to gate the selection of different behaviors in a state-dependent fashion (Weir and Dickinson, 2015) and activation of a single side of the FB induces ipsilateral turning (Guo and Ritzmann, 2013). Horizontal dopaminergic neurons in the FB have been shown to mediate sleep and arousal (Pimentel et al., 2016). The FB receives direct horizontal input from the visual system via the optic glomeruli (Ito et al., 2012) and also from many known modulatory neuropeptidergic neurons (Kahsai et al., 2012; Kahsai and Winther, 2011). The columnar projection neurons coming from the FB likely interact with these horizontal modulatory neurons. Therefore, it is appealing to hypothesize that the FB contains its own bump, downstream of the PB-EB bump, that it uses to integrate navigational information with neuromodulatory signals encoding internal states and sensory inputs.

Acknowledgements

References

Arena, P., Maceo, S., and Patane, L. (2013). A spiking network for spatial memory formation: Towards a fly-inspired ellipsoid body model. *Intl. Joint Conf.. Neural Networks*

Ayroles, J.F., Buchanan, S. M., O'Leary, C., Skutt-Kakaria, K., Grenier, J. K., Clark, A.G, et al. (2015). Behavioral idiosyncrasy reveals genetic control of phenotypic variability. *Proc. Natl. Acad. Sci. U. S. A.* 112, 6706-6711

Berger, S. D., and Crook, S. M. (2015). Modeling the Influence of Ion Channels on Neuron Dynamics in Drosophila. *Front. Comput. Neurosci.* 9, 139.

Bockhorst, T., and Homberg, U. (2015). Amplitude and dynamics of polarization-plane signaling in the central complex of the locust brain. *J. Neurophysiol.* 113, 3291–3311.

Buchanan, S. M., Kain, J. S., and de Bivort, B. L. (2015). Neuronal control of locomotor handedness in Drosophila. *Proc. Natl. Acad. Sci. U. S. A.* 112, 6700-6705.

Chou, Y. H., Spletter, M. L., Yaksi, E., Leong, J. C., Wilson, R. I., and Luo, L. (2010). Diversity and wiring variability of olfactory local interneurons in the Drosophila antennal lobe. *Nat. Neurosci.* 13, 439–449.

Collett, T. S., and Graham, P. (2004). Animal Navigation: Path Integration, Visual Landmarks and Cognitive Maps. *Curr. Biol.* 14, R475–R477.

de Bivort, B. L., and van Swinderen, B. (2016). Evidence for selective attention in the insect brain. *Curr Opin Insect Sci* 15, 9–15.

Domenici, P., Booth, D., Blagburn, J. M., and Bacon, J. P. (2008). Cockroaches keep predators guessing by using preferred escape trajectories. *Curr. Biol.* 18, 1792–1796.

Etienne, A. S., and Jeffery, K.J. (2004). Path integration in mammals. *Hippocampus* 14, 180–192.

Feinberg, E.H., VanHoven, M. K., Bendesky, A., Wang, G., Fetter, R. D., Shen, K., et al. (2008). GFP Reconstitution Across Synaptic Partners (GRASP) defines cell contacts and synapses in living nervous systems. *Neuron* 57, 353–363.

Fruchterman, T., of Computer Science, U. of I. at U.-C. D., and Reingold, E. M. (1990). *Graph Drawing by Force-directed Placement*. Department of Computer Science, University of Illinois at Urbana-Champaign.

Gaudry, Q., Hong, E. J., Kain, J., de Bivort, B. L., and Wilson, R. I. (2013). Asymmetric neurotransmitter release enables rapid odour lateralization in Drosophila. *Nature* 493, 424–428.

Gelfand, M. V., Collins, C. A., and DiAntonio, A. (2008). Visualizing glutamatergic cell bodies and synapses in Drosophila larval and adult CNS. *Journal of Comp. Neurol.* 508, 131-152

Gouwens, N. W., and Wilson, R. I. (2009). Signal propagation in Drosophila central neurons. *J. Neurosci.* 29, 6239–6249.

Guo, P., and Ritzmann, R. E. (2013). Neural activity in the central complex of the cockroach brain is linked to turning behaviors. *J. of Experimental Biol.* 216, 992-1002.

Haferlach, T., Wessnitzer, J., Mangan, M., and Webb, B. (2007). Evolving a Neural Model of Insect Path Integration. *Adapt. Behav.* 15, 273–287.

Heinze, S. (2014). Polarized-Light Processing in Insect Brains: Recent Insights from the Desert Locust, the Monarch Butterfly, the Cricket, and the Fruit Fly. *Polarized Light and Polarization Vision in Animal Sciences* Springer Series in Vision Research., ed. G. Horváth (Springer Berlin Heidelberg), 61–111.

Hodgkin A. L., and Huxley A. F. (1952) A Quantitative Description of Membrane Current and its Application to Conduction and Excitation in Nerve. *The Journal of Physiology.* 117, 500-544.

Homberg, U., Heinze, S., Pfeiffer, K., Kinoshita, M., and el Jundi, B. (2011). Central neural coding of sky polarization in insects. *Philos. Trans. R. Soc. Lond. B Biol. Sci.* 366, 680–687.

Ito, K., Bacon, J. P., and Strausfeld, N. J. (2012). Optic glomeruli and their inputs in Drosophila share an organizational ground pattern with the antennal lobes. *J. Neurosci.* 32 6061-6071

Kahsai, L., and Winther, Å. M. E. (2011). Chemical neuroanatomy of the Drosophila central complex: distribution of multiple neuropeptides in relation to neurotransmitters. *The Journal of Comp. Neuro.* 519, 290-315.

Kahsai, L., Carlsson, M. A., Winther, A. M., and Nässel, D. R. (2012). Distribution of metabotropic receptors of serotonin, dopamine, GABA, glutamate, and short neuropeptide F in the central complex of Drosophila. *Neuroscience* 208, 11–26.

Kasthuri, N., Hayworth, K. J., Berger, D. R., Schalek, R. L., Conchello, J. A., Knowles-Barley, S., et al. (2015). Saturated Reconstruction of a Volume of Neocortex. *Cell* 162, 648–661.

Kim, A. J., Fitzgerald, J. K., and Maimon, G. (2015). Cellular evidence for efference copy in Drosophila visuomotor processing. *Nat. Neurosci.* 18, 1247–1255

Knierim, J. J., and Zhang, K. (2012). Attractor dynamics of spatially correlated neural activity in the limbic system. *Annu. Rev. Neurosci.* 35, 267–285.

Lin, C.-Y., Chuang, C.-C., Hua, T.-E., Chen, C.-C., Dickson, B. J., Greenspan, R. J., et al. (2013). A comprehensive wiring diagram of the protocerebral bridge for visual information processing in the Drosophila brain. *Cell Rep.* 3, 1739–1753.

Liu, W. W., and Wilson, R. I. (2013). Glutamate is an inhibitory neurotransmitter in the Drosophila olfactory system. *Proc. Natl. Acad. Sci. U. S. A.* 110, 10294–10299.

Marder, E. (2011). Variability, compensation, and modulation in neurons and circuits. *Proc. Natl. Acad. Sci. U. S. A.* 108 Suppl 3, 15542–15548.

Martín-Peña, A., Acebes, A., Rodríguez, J.-R., Chevalier, V., Casas-Tinto, S., Triphan, T., et al. (2014). Cell types and coincident synapses in the ellipsoid body of Drosophila. *Eur. J. Neurosci.* 39, 1586–1601.

McNaughton, B. L., Chen, L. L., and Markus, E. J. (2007). "Dead Reckoning," Landmark Learning, and the Sense of Direction: A Neurophysiological and Computational Hypothesis. *J. Cogn. Neurosci.* 3, 190–202.

Mehmet Fişek, and Rachel we Wilson (2014). Stereotyped connectivity and computations in higher-order olfactory neurons. *Nat. Neurosci.* 17, 280–288.

Nagel, K. I., Hong, E. J., and Wilson, R. I. (2015). Synaptic and circuit mechanisms promoting broadband transmission of olfactory stimulus dynamics. *Nat. Neurosci.* 18, 56–65.

Nern, A., Pfeiffer, B. D., and Rubin, G. M. (2015). Optimized tools for multicolor stochastic labeling reveal diverse stereotyped cell arrangements in the fly visual system. *Proc. Natl. Acad. Sci. U. S. A.* 112, E2967–76.

Ofstad, T. A., Zuker, C. S., and Reiser, M. B. (2011). Visual place learning in Drosophila melanogaster. *Nature* 474, 204–207.

Pereda, A. E. (2014). Electrical synapses and their functional interactions with chemical synapses. *Nat. Rev. Neurosci.* 15, 250–263.

Pfeiffer, K., and Homberg, U. (2014). Organization and functional roles of the central complex in the insect brain. *Annu. Rev. Entomol.* 59, 165–184.

Pimentel, D., Donlea, J. M., Talbot, C. B., Song, S. M., Thurston, A. J. F., and Miesenböck, G. (2016). Operation of a homeostatic sleep switch. *Nature* 536, 333–337.

Ratté, S., Hong, S., De Schutter, E., and Prescott, S. A. (2013). Impact of neuronal properties on network coding: roles of spike initiation dynamics and robust synchrony transfer. *Neuron* 78, 758–772.

Rohrbough, J., and Broadie, K. (2002). Electrophysiological analysis of synaptic transmission in central neurons of Drosophila larvae. *J. Neurophysiol.* 88, 847–860.

Rolls, M. M. (2011). Neuronal polarity in Drosophila: sorting out axons and dendrites. *Dev. Neurobiol.* 71, 419–429.

Schneider-Mizell, C. M., Gerhard, S., Longair, M., Kazimiers, T., Li, F., Zwart, M. F., et al. (2016). Quantitative neuroanatomy for connectomics in Drosophila. *Elife* 5, e12059

Seelig, J. D., and Jayaraman, V. (2013). Feature detection and orientation tuning in the Drosophila central complex. *Nature* 503, 262–266.

Seelig, J. D., and Jayaraman, V. (2015). Neural dynamics for landmark orientation and angular path integration. *Nature* 521, 186–191.

Sheeba, V., Gu, H., Sharma, V. K., O'Dowd, D. K., and Holmes, T. C. (2008). Circadian- and light-dependent regulation of resting membrane potential and spontaneous action potential firing of Drosophila circadian pacemaker neurons. *J. Neurophysiol.* 99, 976–988.

Skaggs, W., Knierim, W., and Kudrimoti, H. S. (1995). A model of the neural basis of the rat's sense of direction. *Adv. Neural Inf. Process. Syst.* Vol. 7, ed. G Tesauro, DS Touretzky, TK Leen, pp. 173–78

Solovyeva, K. P., Karandashev, I. M., Zhavoronkov, A., and Dunin-Barkowski, W. L. (2016). Models of Innate Neural Attractors and Their Applications for Neural Information Processing. *Front. Syst. Neurosci.* 9, 178

Song, P., and Wang, X.-J. (2005). Angular Path Integration by Moving "Hill of Activity": A Spiking Neuron Model without Recurrent Excitation of the Head-Direction System. *J. Neurosci.* 25, 1002–1014.

Stanley Heinze, and Uwe Homberg (2007). Maplike representation of celestial E-vector orientations in the brain of an insect. *Science* 315, 995–997.

Stein, R. B. (1967). Some models of neuronal variability. *Biophys. J.* 7, 37–68.

Strausfeld, N. J. (1976). "The Primary Compartments of the Brain," in *Atlas of an Insect Brain*, ed. N. J. Strausfeld (Springer Berlin Heidelberg), 31–40.

Taube, J. S. (2007). The head direction signal: origins and sensory-motor integration. *Annu. Rev. Neurosci.* 30, 181–207.

Weir, P. T., and Dickinson, M. H. (2015). Functional divisions for visual processing in the central brain of flying Drosophila. *Proc. Natl. Acad. Sci. U. S. A.* 112, E5523–32.

Wolff, T., Iyer, N. A., and Rubin, G. M. (2015). Neuroarchitecture and neuroanatomy of the Drosophila central complex: A GAL4–based dissection of protocerebral bridge neurons and circuits. *J. Comp. Neurol.* 523, 997-1037

Varga, A. G., and Ritzmann, R. E. (2016). Cellular Basis of Head Direction and Contextual Cues in the Insect Brain. *Curr. Biol.* 26, 1816-1828

Zhang, K. (1996). Representation of spatial orientation by the intrinsic dynamics of the head-direction cell ensemble: a theory. *J. Neurosci.* 16, 2112–2126.

Table

CX	Central Complex
EB	Ellipsoid Body
FB	Fan-shaped Body
PB	Protocerebral Bridge
E-PG	Ellipsoid Body-Protocerebral Bridge-Gall neurons, projecting from the EB to the PB and Gall. Called PBG1–8.b-EBw.s-D/Vgall.b in Wolff et al., 2015 and "wedge neurons" in Seelig & Jayaraman, 2015.
P-EG	Protocerebral Bridge-Ellipsoid Body-Gall neurons, projecting from the PB to the EB and Gall. Called PBG1–8.s-EBt.b-D/Vgall.b in Wolff et al., 2015.
P-EN	Protocerebral Bridge-Ellipsoid Body-Noduli neurons, projecting from the PB to the EB and Noduli. Called PBG2–9.s-EBt.b-NO1.b in Wolff et al., 2015.
Pintr	Protocerebral Bridge intrinsic neurons. Comprising PB18.s-GxΔ7Gy.b, PB18.s-9i1i8c.b and PBG6–8.sG9.b in Wolff et al., 2015.
PCA	Principle Components Analysis
HD	Head Direction
PSC	Postsynaptic Current

Table 1 – Abbreviations used herein.

Page was left intentionally blank

Chapter III: A circuit bottleneck imparts individuality to context modulation of locomotion

Abstract:

Understanding how the brain generates locomotor behavior is a significant challenge in neuroscience. One of the brain regions involved in *Drosophila melanogaster* is the central complex (CX). Studying the CX is complicated by its diverse roles in many behaviors and in different environments. We exploited idiosyncratic behavioral biases across individual animals to understand how the CX functions under different contexts. Individual *Drosophila* locomoting in a simple Y-shaped maze display individual biases in their preference to turn in one direction or the other, as they repeatedly pass through the center point of the maze. We have recently found that individual biases are context dependent. When flies are exposed to ambient illumination, their locomotor turning bias can dramatically shift to new biases that are different, but not entirely independent of their original bias and are rapidly reversed by turning the illumination off. Here, we have exploited this luminance-dependent modulation to study locomotor control by the protocerebral bridge (PB), which is one of the core neuropils of the central complex. Silencing sub-populations of PB neurons with Shibire[ts], a mutant of dynamin that disrupts vesicular recycling, revealed that the PB drives locomotor control through spatially segregated output neurons while behaving in the light or dark. Furthermore, we have identified output neurons of the PB innervating the lateral accessory lobe that display morphological correlates of light-dependent modulation of locomotor biases, predicted by a model in which PB output neurons directly influence locomotor drive to the right or left.

Introduction:

Locomotion in *Drosophila melanogaster* is generated by the coordinated activity of many regions of the brain. Several attempts have been made to try to identify the neural networks

across the brain that influence locomotor behavior (Dunn et al. 2016; Robie et al. 2017; Venkatachalam et al. 2016; Cande et al. 2018). This is especially difficult for spontaneous locomotion that are not the result of strong stimulation. Previously, we have found idiosyncratic differences in spontaneous behavior in individual *Drosophila melanogaster* flies(Buchanan et al. 2015). When flies were put in Y-shaped mazes, individuals displayed sometimes strongly biased turning behavior (extreme examples would turn right up to 90% of the time). Furthermore, we found that these turn biases could be acutely modulated by silencing neural activity in the Central Complex (CX). We hypothesized that individual flies have stochastic developmental differences that leads to asymmetry in pre-motor circuits. These could be distributed evenly across the brain, or in key choke points, like the CX, that could impart larger biases on individual behavior.

The CX is a deep, midline spanning structure that responds to highly integrated sensory features, motivational state and internal spatial representations(Donlea et al. 2018; Varga & Ritzmann 2016; Weir & Dickinson 2015; Liu et al. 2016; Seelig & Jayaraman 2013). It is composed of four main neuropil, the Ellipsoid Body (EB), Protocerebral Bridge (PB), Fan-Shaped Body (FB), and Paired Noduli (NO) and three tightly coupled adjacent neuropil, the Lateral Accessory Lobe (LAL), Bulb and Posterior Slope (PS), thought to be the primary input and output a   areas of the CX (Wolff et al. 2015). The central complex is thought to underlie the generation of many of the spontaneous behaviors ((Kahsai & Winther 2011)).

The best anatomically described neuropil of the CX thus far is the PB. Previous studies have attempted to comprehensively inventory classes of neurons that innervate the PB ((Wolff et al. 2015; Lin et al. 2013)). They found between 16-18 cell types. These include neurons projecting to other central complex as well as the LAL and PS. The PB and EB are interconnected by a recurrent loop formed by several classes of interneurons that divide both the EB and PB into columns ("wedges" in the EB and "glomeruli" in the PB). These neurons are thought to encode a ring attractor that is used to store a representation of heading, much like the head-direction cells in mammals ((Seelig & Jayaraman 2015; Green et al. 2017; Kakaria &
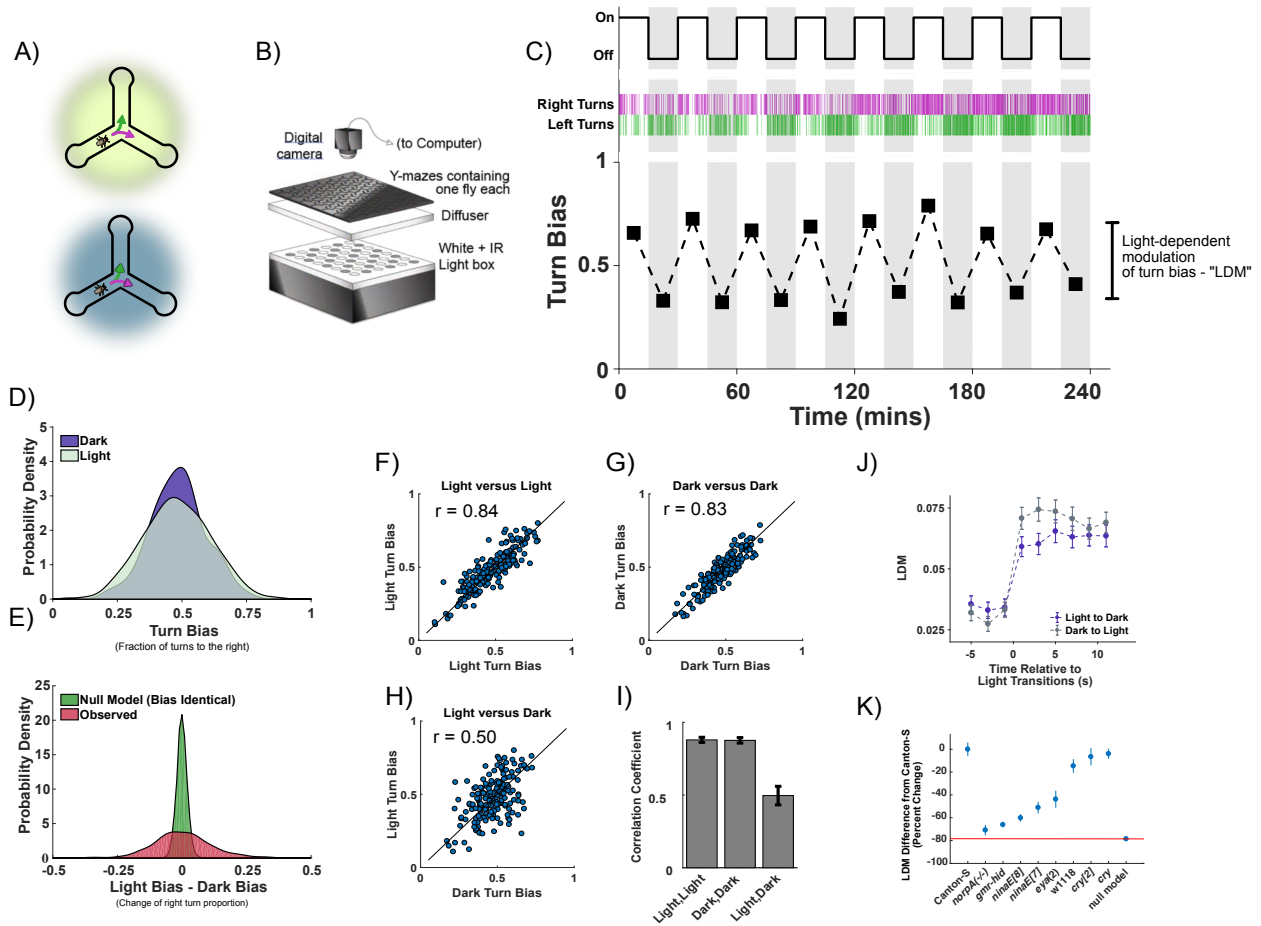
Figure 1: Individual flies display idiosyncratic modulation of turn biases by ambient illumination:
A population of animals were tested for how much their turn biases could be modulated by light. All panels from the same distribution of CS flies, n = 203. (A) Flies were behaving in two ambient luminance conditions: whole field white light illumination or complete darkness. (B) Behavior boxes with white and IR light trans-illumination allowed for continuous centroid tracking in the light and dark. (C) An extreme individual illustrates the LDM phenotype. (top) Luminance condition across the 4 hour experiment (bin size = 15 minutes). (middle) Raster of individual turns (right turns: magenta; left turns: green) as a function of experimental time shows phasic turn probabilities correlated with illumination conditions. (C) Turn bias quantified as proportion of right turns shows that the turn bias toggles between 0.7 and 0.3 phasic-locked to the light condition. (D) Kernel density estimate of the turn bias of the entire population of flies either in the dark or in the light. Population displays no change in median turn bias but an increase in dispersion in the light (med$_{light}$ = 0.47, med$_{dark}$ = 0.48, p = 0.095, vbe$_{light}$=0.096, vbe$_{dark}$ = 0.066, p < 10^-6, n = 203). (E) Kernel density estimates of observed and expected amounts of change of rank order of the distribution of turn biases of individual animals (p = 0.628, student's t test, p < 10^-6, bootstrapped z test, n = 203). (F-I) Light and dark biases were quantified in the first and second two hour period of the experiment. (D) Turn biases only in the light periods (E) dark periods or (F) compared between light and dark (Pearson correlation coefficient, n = 203). (G) Correlation coefficients for each condition in the same animals shows LDM effect across population. (J) Whole field illumination was turned on or off every 60 seconds used to bin turn bias differences between light and dark relative to the light transitions for every individual. Shown is the mean absolute deviation of the differences distribution corrected for the expected dispersion due to sampling error. Error bars represent bootstrap resampled standard errors as described below. (K) Comparison of LDM between photoreceptor or phototransduction mutants. Each LDM is compared to that observed in Canton-S. (p values calculated by 10,000 bootstrap resamples, ▢ = p < 0.05, ▢▢ = p < 0.01, ▢▢▢ = p < 0.001)

de Bivort 2017)). The PB is one of the most derived traits of the insect brain, therefore, we expected the neurons in the PB to participate in multiple decision and spatial guidance pathways. This is supported by decades of studies in CX mutants that show diverse behavioral effects of mutating the PB.

Here we sought to disentangle the roles of the PB using an original method of studying neural circuits. If individual turn biases are generated by differences (coming from developmental stochasticity) in neurons within the PB, then those neurons effects on locomotion may be separable. The CX is innervated by 1000s of input neurons from many diverse sensory pathways. We hypothesized that flies behaving in specific sensory contexts may display differences in individual behavior based on the subset of input neurons involved in generating that behavior. Here, we have found that flies display individual differences in spontaneous locomotor behavior while behaving in different ambient luminance conditions. We found that these differences are mediated by the CX, specifically neurons innervating the PB. Finally, we found that those influences on locomotion can be attributed to different classes of PB neuron.

Results:

Light modulates individual turn biases:

Previously, locomotor biases were shown to be persistent over both short and long time scales in individual flies (However, although these biases are stable over time, they are also dependent on the sensory context in which the animal is behaving (Fig 1A). We found that changing the ambient luminance during behavior (running the experiment in the light or the dark, while tracking the flies with invisible infrared in both conditions) could dramatically change the locomotor bias of individual flies (Fig. 1B-C). Individual locomotor biases in both the light and the dark were broadly distributed with modes of zero bias (equal portion of turns to the left and right; Fig. 1D, SFig. 1A,B,[compare with null models]). But at the level of individual behavior, the bias changed. Sometimes an individual's left (or right) bias in the light would become a

stronger left (or right) bias in the dark. For other individuals, the bias changed sign from left (or right) to right (or left) when the luminance context changed. The difference between the light bias and dark bias for an individual is the Light-Dependent Modulation of turn bias (LDM).

Like the distributions of turn bias in the light and dark (Fig. 1D), the distribution of LDM (the differences between light bias and dark bias) were broadly distributed with a mode of zero. Indeed, the observed LDM distribution was significantly over- dispersed compared to a null model in which the true biases are identical between the light and dark conditions, and any "measured LDM" comes from sampling error (Fig1. E).

To probe the context-dependence of this behavior, we recorded behavior over 4 hours, switching the light on or off every 15 minutes. Turn biases of individual flies were largely persistent across all the light periods and dark periods respectively over short and long timescales (Fig. 1F-G & S.F1**, day to day persistence). Within single multi-hour experiments, the turn bias exhibited at the beginning of the experiment in the light was highly correlated with the turn bias exhibited at the end of the experiment in the light (r=0.84, p<1e-6, n = 398; Fig. 1F). The biases in the dark were likewise correlated (r=0.83, p<1e-6, n=398; Fig. 1G). However, the correlation between the two luminance conditions, was significantly lower (r=0.50, p<1e-6; Fig. 1H). This indicates that the two biases are stable traits of each animal and represent different behavioral states. Importantly, the correlation of turn bias between the light and dark was still quite strong (Fig. 1I).

To begin to understand the circuitry that underlies LDM, we wanted to determine whether it occurred slowly or rapidly. To examine the kinetics of turn bias modulation, we aligned turns that occurred before and after the transitions from dark to light and light to dark (Fig. 1J). We found that LDM occurred rapidly, fully transitioning between light and dark biases after about 5 seconds. This was true regardless of whether the lights were turned on or off. Because the kinetics were fast, we inferred that LDM likely arises in changes in neural dynamics or cell signaling cascades, and not from longer time scale processes like transcription and translation.
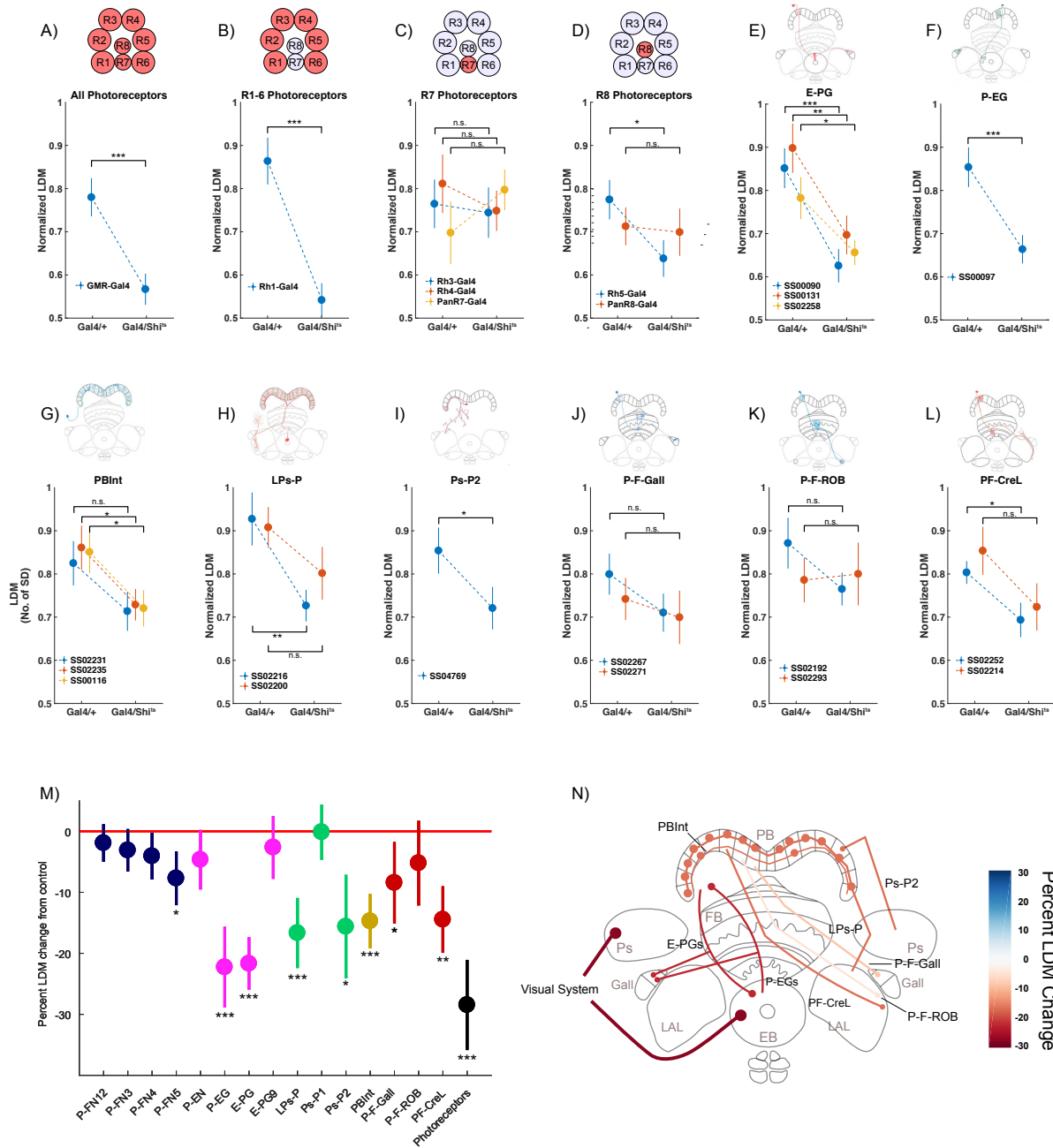
Figure 2: Silencing of neurons in the PB reduces LDM: (A-L) LDM compared at restrictive temperatures between genetic controls, promotor-Gal4/+ and promotor-Gal4/UAS-Shi^{ts}. When multiple Gal4's were tested, each are shown as separate comparisons. (A-D) Gal-4's targeting subsets of the photoreceptors. (A) All photoreceptors (B) Primary photoreceptors [R1-6] (C) UV-sensitive photoreceptors [R7] (D) Blue-Green photoreceptors [R8]. (E-G) Split-Gal4's targeting bump-forming neurons. (H-I) Input neurons from the posterior slope. (J-L) Output neurons projecting to the LAL. (M) Change in LDM compared to genetic control for each neuron type. When multiple Gal4's target the same neuron, LDMs are computed separately for each Gal4 and averaged. (N) Brain schema of simplified neuron types innervating the PB. Neurons are colored by the effect on LDM of silencing them. (p values calculated by 10,000 bootstrap resamples, ▯ = p < 0.05, ▯▯ = p < 0.01, ▯▯▯ = p < 0.001)

Visual inputs are required for LDM:

Because light modulates turn bias on the timescale of seconds, we hypothesized that neural activity in visual pathways mediates LDM. To test this we measured LDM in flies mutant for phototransduction genes. *Drosophila* phototransduction is mediated by 5 different Rhodopsins in photoreceptor cells located in the retina of the compound eye ((Behnia & Desplan 2015)). Loss of function mutants in several of these genes eliminated or reduced LDM. Mutations in *norpA* (which encodes a phospholipase-C required for phototransduction in all photoreceptors (Hardie et al. 2002))*, gmr-hid* (an ectopic eye-specific apoptotic factor that causes developing photoreceptor cell death (Bergmann et al. n.d.)) or *ninaE* (which encodes Rhodopsin1 (Rh1) (O'Tousa et al. 1985)) decreased LDM strongly compared to Canton-S WT flies (effect size = [74%, 68%, 60%], p<1e-6 by 10,000 bootstrap resamples), suggesting that visual input in Rh1 expressing photoreceptors is critical for LDM (Fig. 1K). However, these chronic mutations could have indirect developmental effects across the brain, so these experiments do not definitively implicate neural activity in Rh1-expressing cells as necessary for LDM.

We moved to an inducible neural silencing approach with the thermogenetic effector Shibire[ts], a temperature-sensitive allele of dynamin ((Poodry 1990)). Neurons expressing this effector have normal physiology at the 23°C permissive temperature, but have inhibited vesicular recycling at the 32°C restrictive temperature. We expressed Shibire[ts] in compound eye photoreceptors using the GMR-Gal4 driver (which is expressed in all photoreceptor cells), and ramped the experimental temperature from 23°C to 32°C while recording behavior. We observed a dramatic reduction in LDM as temperatures reached restrictive temperatures (Fig. 2A, Fig. S2**, effect size = 29% reduction, p = 5.9e-5). Likewise, just silencing Rh1-expressing photoreceptors using Rh1-Gal4 to drive Shibire[ts] also reduced LDM (Fig. 2B, effect size = 43%, p < 1e-6) . Silencing R8 cells had a modest effect, suggesting that color vision may play a small role in LDM (Fig. 2C, p=0.14). Silencing Rh3 and 4-expressing photoreceptors had no effect on LDM (Fig 2D, p=0.51), but these rhodopsins are UV- sensitive and our whole field illumination was with white light, so this finding was not surprising.

Neurons in the central complex mediate LDM: Because the bump-forming neurons have been shown to encode a sense of heading in both the light and the dark. We first applied our thermogenetic approach to four types of neurons which likely constitute the core of a ring-attractor circuit that performs angular integration: the E-PGs, the P-EGs, the P-ENs and the PBInt neurons (Kakaria & de Bivort, 2017). To limit off target effects of silencing, we used a collection of sparse split-Gal4 drivers with several lines targeting each cell type (Supp. T1). Silencing two of these classes of neurons (the E-PGs or P-EGs) resulted in a large reduction of LDM (effect size=[23%, 22%], decrease, p=[<1e-6, 3.9e-4], Fig. 2E,F,M). Silencing the PBInt neurons also had a strong effect those of smaller effect size (Fig. 2G; effect size = 15%, p = 0.001) while silencing P-ENs had no effect (Fig. 2M; effect size=3%, p=0.25).

One of the major targets of the ring attractor neurons could be the P-FN neurons which project into the FB and NO and have recently been shown to be functionally connected to both the E-PGs and PBInt neurons (Franconville, 2018). These neurons have been suggested to be involved in navigation by path integration, a plausible mechanism of guiding behavior differently in the absence of visual cues (Stone 2017). Therefore, we next tested whether silencing these neurons also reduced LDM. We found that silencing most P-FN classes had no effect on LDM. However, silencing one class, the P-FN5 cells, did result in a modest decrease in LDM (Fig. 2M effect size=6%, p=0.035).

In addition to the bump-forming neurons, there are three other putative input neurons to the PB, all of which have dendrites in the PS. To test the hypothesis that multiple input pathways could lead to LDM, we next sought to determine whether any of these neurons also played a role in LDM. Of these three input classes, we found that silencing two of them strongly reduced LDM, both the LPs-Ps and the Ps-P2s (Fig. 2H,I,M; effect size=[18%, 17.5%], p=[0.0015, 0.03]).

Because the CX has no direct descending neurons into the VNC, it influences behavior indirectly through its downstream neurons, likely through a set of LAL projection neurons. The
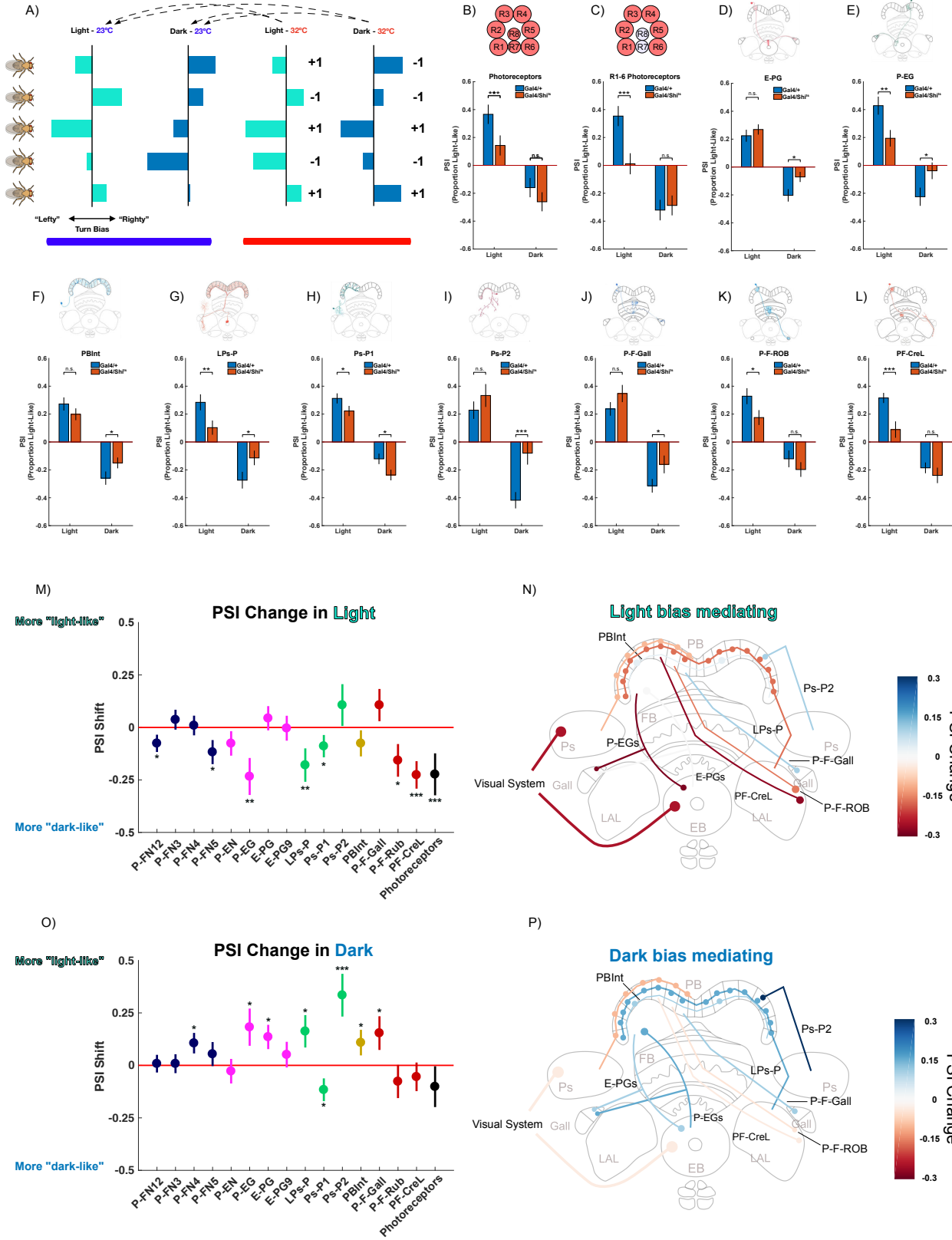
PB only has 5 output neuron classes (E-PGs and P-EGs as discussed above, P-F-galls, P-F-ROBs and PF-CreL) , defined as neurons that send projections to areas besides the FB, EB or No and all 5 of these classes send projections to different domains of the LAL (Lin 2013, Wolff 2015). Silencing the P-F-galls modestly decreased LDM effect, while silencing PF-CreL neurons showed a larger reduction (Fig. 2; effect size=[8%,15%],p=[0.04,0.008]). When we silenced P-F-ROB neurons, we saw mixed effects with each split-gal4, but neither significantly affected LDM.

Taken together, we found that some but not all PB neurons (bump-forming, PS inputs and at least one LAL output) were important in LDM (Fig. 2N) while interneurons between the PB and FB had no effects.

PB circuit elements contribute to LDM in a luminance dependent manner:

Reduction of LDM from thermogenetic inactivation of circuit elements could come about in a range of ways. At one extreme, turning off a circuit element could make the flies' dark bias similar to that of their light bias when those neurons are operating normally. This would be expected if neural activity in that circuit element mediates dark-specific behavioral biases. Conversely, turning off an element could make flies' light bias more similar to that of their dark bias at the permissive temperature, indicating that those neurons mediate light-specific biases. Intermediate effects between these two extremes are possible as well. We quantified the extent to which a thermogenetic manipulation made the profile of biases across populations of flies in the light and the dark more "light-like" or "dark-like" using a metric called the Pre-temperature

Figure 3: Neurons within the PB have luminance specific roles in modulating turn bias: (A) PSI is calculated by comparing restrictive turn biases to permissive turn biases. Turn biases more similar to permissive light biases are scored as a +1 while those more similar to dark biases are scored as -1. If a neuron is targeted by more than 1, they are combined by averaging across each Gal4. (B-C) Gal4's targeting primary photoreceptors show light-specific PSI. (D-F) Bump-forming neurons primarily affect the dark-specific PSI. (G) Dopaminergic large field input neuron affects both light and dark PSI. (H-I) two classes of PS input neurons show opposite PSI shifts. (J-L) Output neurons innervating different regions of the PS show different effects on PSI. (M) PSI shifts in the light for each neuron type compared to genetic control. Gal4's are averaged and then compared to genetic controls. (N) Brain schema colored by light PSI shifts when silencing each neuron class. (O) PSI shifts in the dark for each neuron type compared to genetic controls. (P) Brain schema colors by dark PSI shifts when silencing each neuron class.

Similarity Index (PSI; see Methods, Fig 3A). Positive values of PSI indicate that at the restrictive temperatures, the turn bias is more light-like than dark-like; while negative scores indicate the opposite.

As expected, silencing photoreceptors (either GMR-Gal4 or Rh1-Gal4) shifted the light bias to be more dark-like (Fig. 3B,C). On the other hand, silencing E-PGs shifted the dark bias to be more light-like (delta PSI=0.12, p=0.013, Fig. 3D,O). Interestingly, we observed no effect on the light biases when these neurons were silenced. These data suggested that E-PGs mediate the biases of the fly only in dark and not the light. Silencing P-EGs had a similar effect on dark biases (delta PSI=0.2, p=0.018, Fig. 3E,O). In contrast to the E-PGs however, silencing the P-EGs also affected light biases by making them more dark-like (delta PSI=-0.24, p=0.007; Fig. 3E,M). This suggested that activity in P-EGs could mediate the turn bias exhibited in both the light and the dark. Silencing PBInts also shifted the dark biases to be more like the light biases (delta PSI=0.11, p=0.023; Fig. 3F,O). However, silencing the P-ENs had no significant effect on either the dark bias or the light bias (Fig. 3M,O). These results suggest a tight functional relationship between E-PGs, P-EGs and PBInts (but not P-ENs) in mediating individual context-dependent locomotor biases.

While the bump-forming neurons mediate only the dark bias, the PS inputs are mixed. Silencing the Ps-P1 neurons changed both the light and dark bias to be more light-like (delta PSI=[-0.12,-0.13], p=[0.023,0.009]; Fig. 3H,M-P). Because the effects are in the same direction, we had not previously noted that they were involved in generating LDM. Silencing Ps-P2 neurons strongly shifted the dark bias to be more light like, similarly to silencing the bump-forming neurons(PSI=[0.10,0.31], p=[0.09,3.4e-4], Fig. 3I,M-P). Silencing LPs-L neurons made both the light bias more dark-like and the dark bias more light-like, similar to the P-EG neurons (delta PSI=[-0.18,0.21], p=[0.023,0.009]; Fig. 3G,M,O). From these data we concluded that PS neurons have a role in mediating both the light-bias and dark-bias, segregated into the activity of the Ps-P1 and Ps-P2 neurons. These data also suggested that LPs-P neurons play a role in generating both biases.

77
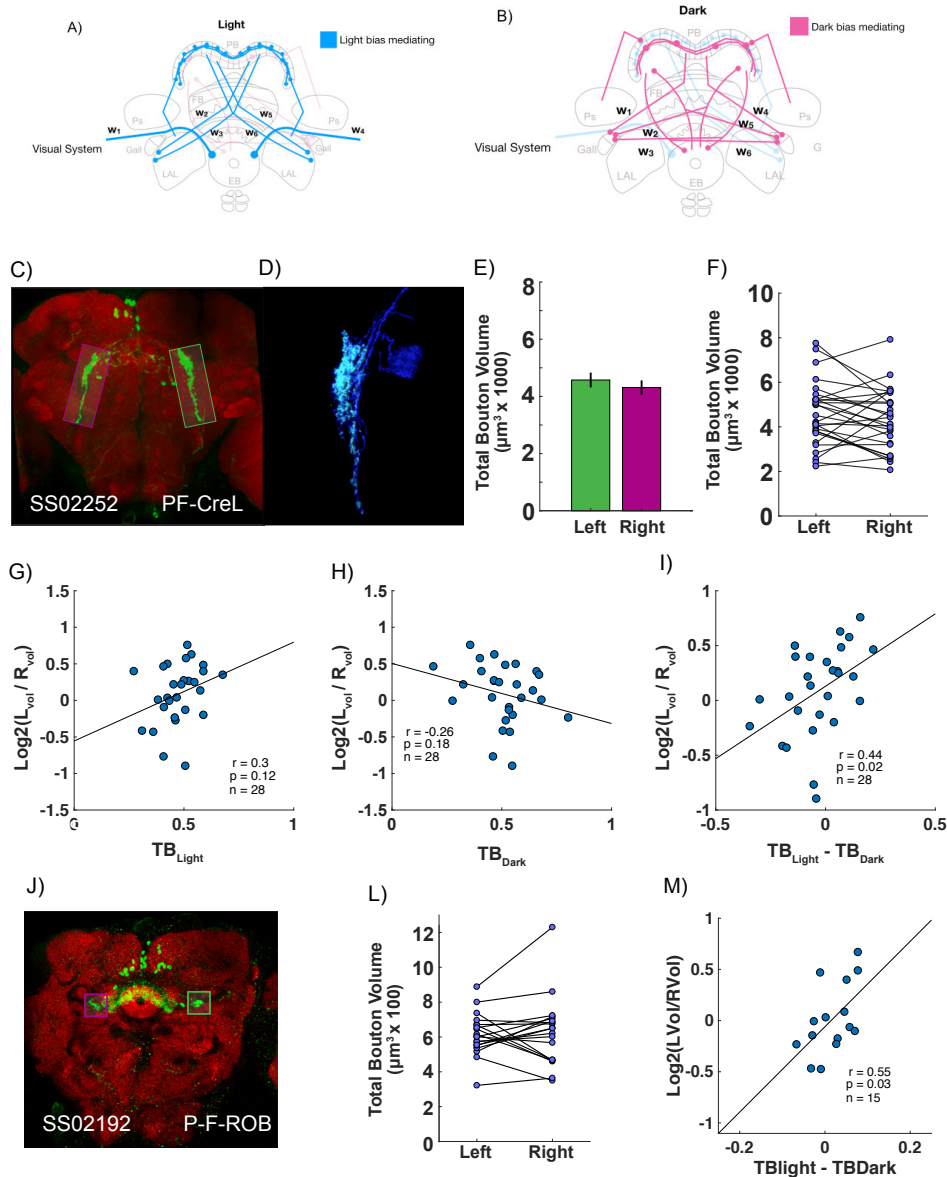
Figure 4: Output neuron pre-synaptic volumes are predictive of LDM: (A-B) Models of how asymmetries in light-bias and dark-bias mediating circuitry could lead to LDM. Neuron pairs with asymmetric weights could propagate those asymmetries into pre-motor circuits. (C) Max z-projection of pre-synaptic PF-CreL neurons (SS02252-Gal4 / UAS-BrpShort::mStraw; nc82 - red, anti-mStraw - green). (D) Close up of pre-synaptic region of PF-CreL neurons. (E) Average bouton volume of PF-CreL neurons innervating the left and right lateral LALs. (F) Paired bouton volumes show considerable variability of volumes on left and right. (G-H) Scatter plots between individual turn biases in the light or dark and the ratio of bouton volumes between the two sides. (I) Scatter plot between individual LDMs and the ratio of bouton volumes (r = 0.44, p = 0.02, n = 28). (J) Max z-projection of pre-synaptic P-F-ROB neurons (SS02192-Gal4 / UAS-BrpShort::mStraw; nc82 - red, anti-mStraw - green). (K) Average bouton volume of PF-CreL neurons innervating the left and right lateral LALs. (L) Paired bouton volumes show considerable variability of volumes on left and right. (M) Scatter plot between individual LDMs and the ratio of bouton volumes (r = 0.55, p = 0.03, n = 15).

Because we found that certain neurons affect light biases while others affect dark biases, we were interested in whether we would observe a similar separation in the output neurons. We have previously found that silencing two neurons projecting to gall (E-PG, P-EG) selectively shifted the dark bias to be more light-like (Fig. 3D,E). Silencing another gall projecting neuron (P-F-gall) also shifted the dark bias to be more dark like (delta PSI=[0.1,0.15], p=[0.08,0.34], Fig. 3J,M-P). In contrast, silencing the LAL projecting neurons selectively shifted the light bias to be more dark like (P-F-ROB: delta PSI=[-0.15,-0.04], p=[0.038,0.09] or P-CreL: delta PSI=[-0.25,-0.035], p=[3.5e-4,0.21], Fig. 3K,L,M-P). These data suggested that the spatial separation of circuit elements determines whether those output neurons influence the dark bias or the light bias (Fig. 3N,P).

Morphology of PB output neurons suggests they bias behavior asymmetrically:

The observation that turn biases are be different in the light and dark suggested an asymmetry somewhere in pre-motor circuitry. If LDM was generated from different subsets of neurons mediating each bias, we hypothesized that this could arise due to asymmetries in the weights of the output neurons of the PB (the E-PGs, P-EGs, P-F-galls, P-F-ROBs and PF-CreLs). For example, an animal with more excitable output neurons innervating the left hemispheric gall (via any of the E-PG, P-EG of P-F-gall populations) compared to the right hemisphere could drive an animal to be more left biased in the dark (Fig. 4A,B). That same animal could equal, symmetric outputs projecting to the lateral LAL (via P-F-ROB or PF-CreL populations). Therefore, that animal would make more left turns in the dark and more balanced turning behavior in the light, hence we would observe LDM in that animal. We hypothesized that asymmetric weights of these neurons could be generated by several cell intrinsic qualities of these neurons (differences in excitability, synaptic strength or total synapse volume) or they could be inherited by upstream neurons. All of these mechanisms should have lead to LDM if our hypothesis was correct. Because we needed to sample from an entire population of LDM

79

flies, we turned to investigating total synaptic volume of subclasses of tese neurons by quantifying the volume of pre-synapses.

We first chose to test the PF-CreL reasons. First, they showed a strong LDM and PSI phenotype. Second, they represented a small population of cells (only 7 cells on each side of the brain) so differences in their morphology could have a larger impact on the turn bias (Fig. 4C). Third, they had large pre-synaptic arbors that likely have increased variability in volume and by extension, synaptic weights (Fig. 4D). We found that the average fly had the same volume of pre-synapses on the left and right side of the brain (Fig. 4E). However, we observed that in some flies there was considerable differences between the volume on the left and right (Fig. 4F). When we compared the volumes on the two sides of the brain, we found that the ratio of synaptic volumes between the two hemispheres was significantly correlated with LDM (r=0.44, p=0.02, n=28, Fig. 4I). In addition we found evidence the suggest a correlation between the ratio and the light bias and a negative correlation between the ratio and dark bias, although those correlations were not significant (Fig. 4G,H). We next decided to examine the P-F-ROB neurons as they had similar silencing phenotypes in LDM and PSI to PF-CreL neurons. We again found considerable asymmetries in synaptic volumes and a significant correlation between these asymmetries and LDM (r=0.55, p=0.03, n=15; Fig. 4 J-M). These data suggested to us that both of these neuron classes were able to impart asymmetry to the locomotor behavior due to structural differences in their pre-synaptic arbors.

Discussion:

Individual flies can have dramatically strong LDM of individual turn biases between the light and in the dark. We found that neurons projecting into, out of and locally within the PB mediate LDM, but in specific ways depending on cell type. Some neurons, photoreceptors, one class of PS input and LAL projections, seemed only to influence behavior in the light. Others, bump-forming neurons (E-PGs), a different class of PS input and another GA projecting neuron only influence turn biases in the dark. Finally, several neurons of the PB modulated both the

light and dark bias, including a dopaminergic neuron that is well positioned to be the switch that could modulate the entire circuit.

Interestingly, we found that the dark bias and the light bias are strongly correlated (Fig 1H). This suggested to us that locomoting in the light and dark were not independent of each other and instead converged on common circuits. Our perturbation experiments suggested that this occurs downstream of the CX. We found that silencing output neurons did not show mixed effects (affects on both the light and dark bias) as would be expected if we were targeting common circuit elements (Fig. 3N,P). Instead, our results suggest that the PB is gating the activity of these sub-circuit elements between the light and the dark. Silencing the E-PGs (bump-forming neurons, Fig. 3D) affects only the dark and not the light bias, this suggests that the fly's internal representation could be dispensable for guiding locomotion in the light. Perhaps this is due to the constant, high fidelity visual cues present to guide the animal. We therefore predict that varying the visual environment to make it less reliable to the animal, could drive the flies to rely more on their internal representation, even in the presence of light, which would reduce LDM.

Several classes of PB neurons do have effects on both light bias and dark bias (Fig. 3N,P). Notably the LPs-P dopaminergic projection neuron from the LAL and PS that projects into the entire PB (Fig. 3G). Dopamine has been shown to have diverse effects on synaptic activity and could represent the gating neuron in this circuit. Two of the bump-forming neurons also seem to play a role in the light bias so those neurons may be directly modulated by the dopaminergic neuron or have distinct roles in each context. Because we saw the perturbation to both biases, however, it suggests that perhaps the activation level is important for proper gating. We would predict that a more graded dissection of the silencing and activation of the dopamine neuron or careful titration of dopamine could reveal an effect on only one bias or the other.

The LAL may be have regional influences on luminance-dependent locomotion. We found that silencing output neurons that innervated the GA disrupted the dark bias, while silencing output neurons projecting to main LAL disrupted the light bias (Fig. 3N). Therefore, we

hypothesize that neurons projecting to the GA promote using the ring attractor to guide behavior while those that project to LAL promote circumventing it. Our morphology data suggests that the LAL projecting neurons either directly stimulate pre-motor pathways, or gate the activity of pre-motor neurons more on one side than the other. In order for asymmetry in the output neurons of the CX to affect behavior they need to be propagated throughout the descending neuron (DNs). The LAL has a limited number of descending neurons, however it has considerable connectivity with the PS. DNs projecting from the PS make up about 35% of all the DNs in the brain with about 75% of those being post-synaptic in the PS and pre-synaptic in the VNC, and are largely ipslateral after the PS((Namiki et al. 2017)),.

In this study, we applied an original approach to studying circuit function. Much as a geneticist would use genetic variability across a population of animals to hypothesize how genes come together to form molecular pathways, we have used individual behavioral variability to determine differences in neural circuits. The advantage of this technique is that we can study the architecture of primarily intact circuits. This was especially useful in this case because we had access to both states of the network. Because of this convergence we can tease apart the neuronal function without even observing any mean shift in behavior. Using this approach we made a formed a strong hypothesis about neural switch mediating different guidance modes of locomotor exploration. Although this particular example required significantly genetic tools, we believe that this sort of approach could be applicable to any population in which one can quantify behavior with sufficient representation of the population statistics.

Neuron Target (Wolff name)	Colloquial Name	Gal-4 Driver
PBG2-9.s-FBl1.b-NO3P.b/PBG2-9.s-FBl1.b-NO3M.b	P-FN1/2	SS02207, SS00425, SS00044, SS02221, SS02304, SS00418, SS00279

PBG2-9.s-FBl2.b-NO3A.b	P-FN3	SS00079, SS00406, SS02255, SS02221, SS00007, SS02304, SS00083
PBG2-9.s-FBl3.b-NO2D.b	P-FN4	SS00161, SS00078, SS00019, SS00082, SS00083
PBG2-9.s-FBl3.b-NO2V.b	P-FN5	SS02243, SS02209, SS02211, SS00082
PBG2-9.s-EBt.b-NO1.b	P-EN	SS02241, SS02268, SS02232
PBG1-8.s-EBt.b-D/Vgall.b	P-EG	SS00097
PBG1-8.b-EBw.s-D/Vgall.b	E-PG	SS00090, SS00131, SS02258
PBG9.b-EB.P.s-ga-t.b	E-PG9	SS04781, SS04782, SS02374
PB.s-FBl6.b.s.l3.s-Vga-s.b	P-F-gall	SS02267, SS02271
PBG1-8.s-FBl3,4,5.s.b-rub.b	P-F-ROB	SS02192, SS02293
PBG1-7.s-FBl2.s-LAL.b-cre.b	PF-CreL	SS02252, SS02214
PB.b-LAL.s-PS.s	PsL-PB	SS02216, SS02200
PBG6-8.sG9.b	PBCap	SS04775
PB18.s-Gx_7Gy.b/PB18.s-9i1i8c.b	PBInt	SS02231, SS02235, SS00116
PBG1/2-9.b-SPSi.s	Ps-P	SS02296, SS00155, SS00153
PBG2-9.b-IB.s.SPS.s	Pslb-P	SS04769

Methods:

Fly Care. Fly lines were housed on standard Bloomington type A corn meal food made in the fly facility at Harvard Bio Labs and stored in temperature-controlled Percival incubators. The incubators were maintained at ~40% relative humidity year round with a 12-h/12-h light-dark cycle with white LED illuminators. On a daily basis, F1's were collected from 25mL fly food bottles and stored in cohorts of ~30 flies for ~4 days until testing to ensure that all animals used

in this study were 4-8 days old. For the screening experiments, 10 virgin females were crossed with 5 males and kept for 24 hours in a food vial to allow all virgin females to be fertilized before successively transferring all parents to two 25 mL fly food bottles 48 hours each. The UAS-Shibire construct was outcrossed for 10 generations into a common lab background strain IsoKH11, the same strain used for genetic controls, by 10 generations of successive backcrosses.

Automated Behavioral Tracking: Video was captured at 1280*960 REFREF at 6-10 fps Point Grey Firefly MV cameras (FMVU-13S2C-CS LINK?REFREF) with illumination as described below**.** All behavior was tracked using the Autotracker package (REFREF). Briefly, regions of interest are defined by the outline of each maze in the array. Next a reference is subtracted across the whole image and flies are detected by changes in the difference image. The video is typically not captured during these experiments and instead only the centroid position is saved.

Behavioral quantification: For all experiments, overall bias was calculated by calculating choice-point transits as the flies move through the maze. Turns are counted when a fly enters the choice point and exits into a different arm than the one it entered. Because of the latency of calling turns compared to the time the decision is actually made, the turn time stamp is adjusted back to the time in which the fly was the closest to the choice point before walking down one of the arms. Often, behavior was recorded across many bins of changing light conditions. In this case, turns were pooled for the appropriate condition across these separate bins. The extent of light-dependent modulation of turn bias is calculated as follows:

$$\text{LDM} = \frac{1}{n} \sum |\text{TB}_{\text{light}} - \text{TB}_{\text{dark}}|$$

The direction of the light-dependent modulation was calculated as follows:

$$\text{PSI} = \frac{1}{n} \sum \text{TB}_{\text{score}}$$

$$\text{TB}_{\text{score,light}} = \begin{bmatrix} \text{if} & |\text{TB}_{\text{light},32} - \text{TB}_{\text{light},23}| > |\text{TB}_{\text{light},32} - \text{TB}_{\text{dark},23}| = 1 \\ \text{else} & |\text{TB}_{\text{light},32} - \text{TB}_{\text{light},23}| < |\text{TB}_{\text{light},32} - \text{TB}_{\text{dark},23}| = -1 \end{bmatrix}$$

$$\text{TB}_{\text{score,dark}} = \begin{bmatrix} \text{if} & |\text{TB}_{\text{dark},32} - \text{TB}_{\text{light},23}| > |\text{TB}_{\text{dark},32} - \text{TB}_{\text{dark},23}| = 1 \\ \text{else} & |\text{TB}_{\text{dark},32} - \text{TB}_{\text{light},23}| < |\text{TB}_{\text{dark},32} - \text{TB}_{\text{dark},23}| = -1 \end{bmatrix}$$

Where TB_{light} and TB_{dark} are the z-scored proportion of right turns in either the light or the dark.

Maze Fabrication. Mazes were cut into 1/16-in.-thick black acrylic using a laser engraver (Epilog). Each arm of a maze was 0.37 in. long and 0.13 in. wide. To inhibit the flies from flipping upside down, the floors of the mazes were lightly roughened with a random orbital sander and fine-grit sand paper, and clear acrylic lids (one per maze) were lubricated with Sigmacote (Sigma). A diffuser made of two sheets of 1/4-in.-thick clear acrylic roughened on both sides by orbital sanding, placed between the LED array and the maze array, provided near-uniform illumination of each maze.

Illumination. A two color LED array with infra-red, centered at 850 nm**, and white LEDs, fabricated by Knema, provided illumination for the maze array. These LED arrays allowed independent control of each channel for constant IR illumination for machine vision and controllable white light illumination. Light intensity was set by 8-bit pulse-width modulation (PWM) of a transistor (**) gating power to the white LEDs using an Arduino Uno with custom control software. A calibration between light intensity and PWM was measured using a ** power meter and total lumens was integrated across (a range of wavelength**).

Thermogenetic Silencing Screen. Flies for screening were recorded continuously during low and high temperature locomotion as well as the ramping period. Four arrays were run simultaneously within a Harris Environmental System that allows for rapidly changing the ambient room temperature. The animals locomoted at the permissive 23º C for 60 minutes, followed by a 60 minute ramping period from the permissive to restrictive temperature 23º C to 32º C, followed by a 60 minute period at the restrictive 32º C. The ramping period is relatively

long to allow sufficient time for heating the relatively low thermal conductance of the acrylic mazes.

References:

Behnia, R. & Desplan, C., 2015. Visual circuits in flies: beginning to see the whole picture. *Current opinion in neurobiology*, 34, pp.125–132.

Bergmann, A. et al. 1998, The Drosophila gene hid is a direct molecular target of Ras-dependent survival signaling. *Cell,* 95(3), pp. 331-341

Buchanan, S.M., Kain, J.S. & de Bivort, B.L., 2015. Neuronal control of locomotor handedness in Drosophila. *Proceedings of the National Academy of Sciences of the United States of America*, 112(21), pp.6700–6705.

Donlea, J.M. et al., 2018. Recurrent Circuitry for Balancing Sleep Need and Sleep. *Neuron*, 97(2), pp.378–389.e4.

Green, J. et al., 2017. A neural circuit architecture for angular integration in Drosophila. *Nature*. 546, pp. 101-106

Hardie, R.C. et al., 2002. Molecular basis of amplification in Drosophila phototransduction: roles for G protein, phospholipase C, and diacylglycerol kinase. *Neuron*, 36(4), pp.689–701.

Kahsai, L. & Winther, A.M., 2011. Chemical neuroanatomy of the Drosophila central complex: distribution of multiple neuropeptides in relation to neurotransmitters. *Journal of Comparative Neurology*, 519(2), pp. 290-315

Kakaria, K.S. & de Bivort, B.L., 2017. Ring Attractor Dynamics Emerge from a Spiking Model of the Entire Protocerebral Bridge. *Frontiers in behavioral neuroscience*, 11(8)

Lin, C.Y. et al., 2013. A comprehensive wiring diagram of the protocerebral bridge for visual information processing in the Drosophila brain. *Cell Reports*, 3(5), pp. 1739-53

Liu, S. et al., 2016. Sleep Drive Is Encoded by Neural Plastic Changes in a Dedicated Circuit. *Cell*, 165(6), pp.1347–1360.

Namiki, S. et al., 2017. The functional organization of descending sensory-motor pathways in Drosophila. *bioRxiv*, p.231696.

O'Tousa, J.E. et al., 1985. The Drosophila ninaE gene encodes an opsin. *Cell*, 40(4), pp.839–850.

Poodry, C.A., 1990. shibire, a neurogenic mutant of Drosophila. *Developmental biology*, 138(2), pp.464–472.

Seelig, J.D. & Jayaraman, V., 2013. Feature detection and orientation tuning in the Drosophila central complex. *Nature*, 503(7475), pp.262–266.

Seelig, J.D. & Jayaraman, V., 2015. Neural dynamics for landmark orientation and angular path integration. *Nature*, 521(7551), pp.186–191.

Varga, A.G. & Ritzmann, R.E., 2016. Cellular Basis of Head Direction and Contextual Cues in the Insect Brain. *Curr Biol*, 26(14), pp.1816–1828.

Weir, P.T. & Dickinson, M.H., 2015. Functional divisions for visual processing in the central brain of flying Drosophila. *Proceedings of the National Academy of Sciences of the United States of America*, 112(40), pp.E5523–32.

Wolff, T., Iyer, N.A. & Rubin, G.M., 2015. Neuroarchitecture and neuroanatomy of the Drosophila central complex: A GAL4-based dissection of protocerebral bridge neurons and circuits. *Journal of Comparative Neurology*, 523(7), pp.997–1037.

Conclusion:

I have investigated the establishment and control of locomotor biases in individual fruit flies. In the early part of my Ph.D. We found that certain genetic elements are associated with the dispersion of the distribution of turn biases across a population of flies. Furthermore, we found that disruption of the expression of a synaptic reinforcement molecule during pupation was sufficient to increase the dispersion of turn biases in a population of flies. Next, we modeled a network of neurons innervating the protocerebral bridge (PB) and ellipsoid body (EB) as a leaky-integrate and fire network using known innervation patterns. We showed that all-to-all connectivity with inhibitory local neurons would form a ring-attractor under many synaptic weight parameters, suggesting a robustness built in to the connectivity of these neuropil. Finally, we have found that locomotor handedness is not a permanent trait but can be rapidly and stably changed by the presence or absence of light. These individual changes represent a reordering of locomotor bias within a nearly identical distribution. This finding represents a new understanding of the definition of individuality that implies that individuals will display distinct behavioral biases under different conditions. Furthermore, we have demonstrated a strategy of applying behavioral individuality as a kind of circuit-wide association study to implicate the function of different neural classes within the PB in controlling locomotor behavior either in the light or the dark. Through this approach we suggest that the PB acts as a gate on the influence of the PB ring attractor circuit in the two sensory conditions.

During development, *D. melanogaster* neurons must accomplish several vital tasks as they move from cell birth to their final adult form (Kohsaka et al. 2012; Spindler & Hartenstein 2010). Each precursor cell must migrate to the appropriate location, terminally differentiate into their eventual cell type, project into the appropriate neuropil and make selective and appropriately weighted synapses with target cells in these compartments. Each of these steps involve a large number properly balanced permissive and restrictive cues. Although many of the factors involved in synapse formation are not yet understood, there is no doubt that many gene

products are required for proper cell targeting and appropriate synaptic weighting. In our study, we have implicated a number of putative synaptic reinforcement molecules that are critical to properly balancing locomotor bias, including the teneurin's. These proteins have been shown to be involved in trans-synaptic partner matching with a number of different matching rules (Hong et al. 2012; Mosca & Luo 2014). If the expression of one of the teneurin genes, *teneurin-a,* is disrupted during pupation by expression of a short-hairpin RNA that is anti-sense to the *teneurin-a* gene, we have shown that animals become more biased on average. This implies that the critical stage of reforming synapses after they retreat at the beginning of pupation is important in limiting the locomotor bias distribution for individual flies. This study does not, however, show which neurons are important in this effect or whether it could be distributed across the whole brain as the RNAi presumably effects all cells that express *teneurin-a* in the animal.

The neurons identified to control the magnitude of individual biases acutely are primarily part of a circuit that was recently shown to project recurrently from the EB to the PB that appear anatomically as a ring were recently shown to encode an egocentric heading as a bump of activity around that ring (Green et al. 2017; Seelig & Jayaraman 2015; S. S. Kim et al. 2017). These neurons represent a midline-spanning circuit that must balance inputs coming from both sides of the brain. Recently, Wolff et al described 16 different cell types that innervate the PB (Wolff et al. 2015). In an attempt to gain an understanding in how this circuit is actually computing this bump of activity, we used their set of neural projection annotations, along with empirically derived neural activity parameters, an all-to-all connectivity assumption and an assumption that local neurons were inhibitory, to generate an integrate-and-fire model of the PB->EB circuit. We found that when our model was challenged with simulations of all of the experimental paradigms previously tested it recreates all of the experimental observations that were seen in the intact circuit in an awake behaving fly. We found that the synaptic weights were robust and could be varied dramatically between neuron classes without affecting the ring-attractor dynamics of the circuit. These results suggest that these ring attractor neurons robustly

form a ring over an variety of developmental configurations and may represent a primitive computational unit that could be redeployed for different functions.

The central complex is a point of high convergence in the central brain of *Drosophila.* It sends projections into the lateral accessory lobe (LAL), an input and output region of the central complex. By exploiting ambient luminance conditions we have shown that individual flies can display drastically different locomotor biases in the dark and light. Furthermore, we have shown that the PB segregates its influence on locomotor behavior into different neurons that project to the LAL. We hypothesize that the influence by these neurons on behavior is likely gated by whether or not they are using their internal compass to mediate behavior. The difference between these two conditions is that in the light the fly can see the walls and floor of the maze as high fidelity visual features so can use edge detection and motion vision to guide their behavior in the light. In the dark the fly must rely on its internal representation, corrected by mechanical cues.

These findings change our perspective on individuality, showing it to be context dependent and not permanent, likely due to differences in neuronal activity in separate circuits involved in the generation of same behavior under different contexts. Furthermore, it represents a novel approach in studying neural circuits. Instead of silencing neurons and looking for mean effects on behavior across animals such as loss of function, this approach reveals subtle neuronal control of behavior by maintaining individual identity across conditions. I believe that this approach may be a promising one for untangling the effect of different neural populations in generating behavior under different conditions.
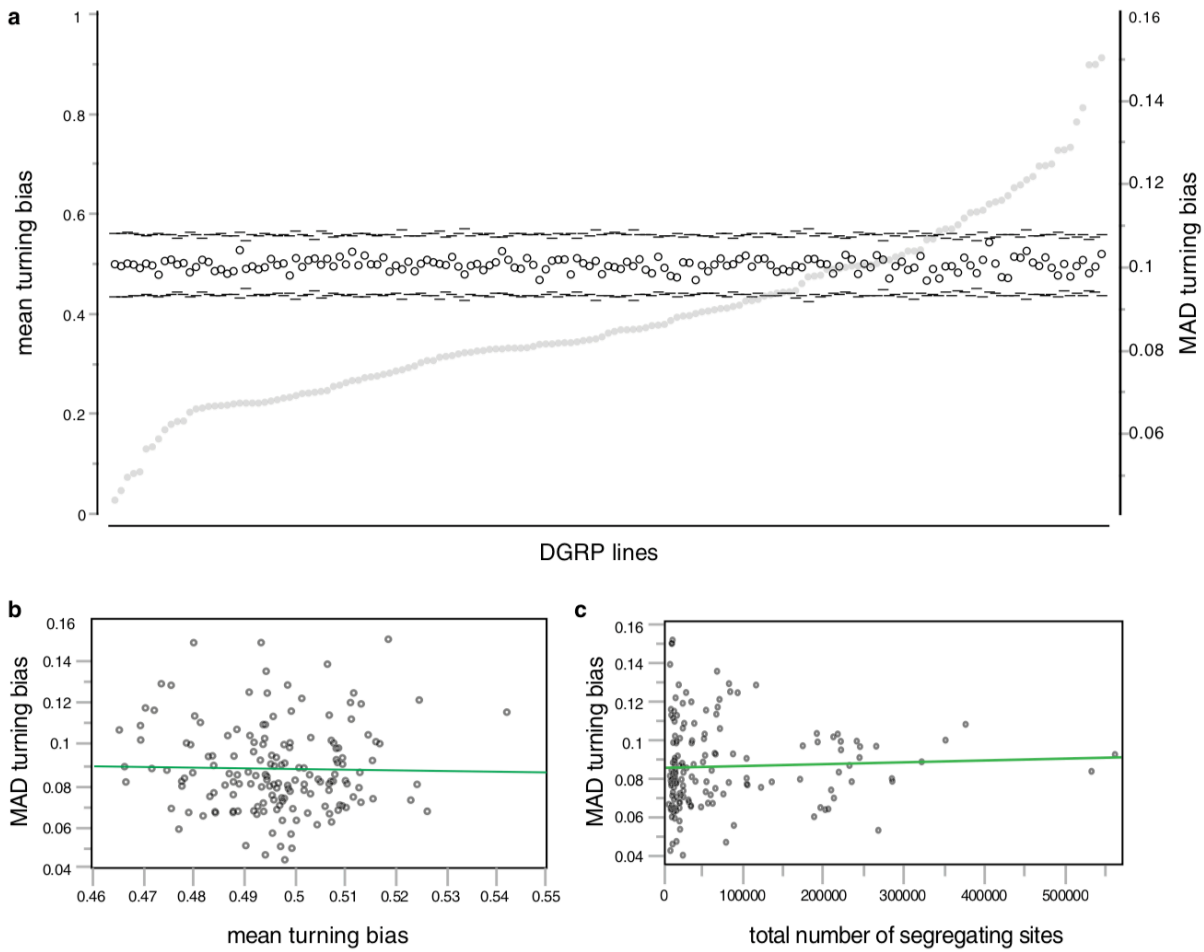
Fig. S1: Turn bias variability is correlated neither with the mean of turning bias nor residual genetic variation within line.
A. Distribution of the mean turning bias for each line, ranked by the MAD of turning bias (grey dots, scale on the right axis). Tick marks represent a 99.9% CI around the mean. There is no significant difference between lines in mean turning bias. Each lines are on average un-handed, making equal portions of left and right turns. ANOVA p-value < 0.87. **B**. No relationship between the mean turning bias and intragenotypic variability (r^2 = 0.0004, p-value = 0.80). **C**. No relationship between intragenotypic variability and residual genetic variation segregating within line (r^2 = 0.0005, p-value = 0.78).

Fig. S2: No genetic variation segregating *within* lines is associated with turning bias.
Crosses between extreme left turning parents (at left) and crosses between extreme right turning parent
(at right) produce unbiased F1 with a 50/50 left-right turning bias. Data modified from[4].

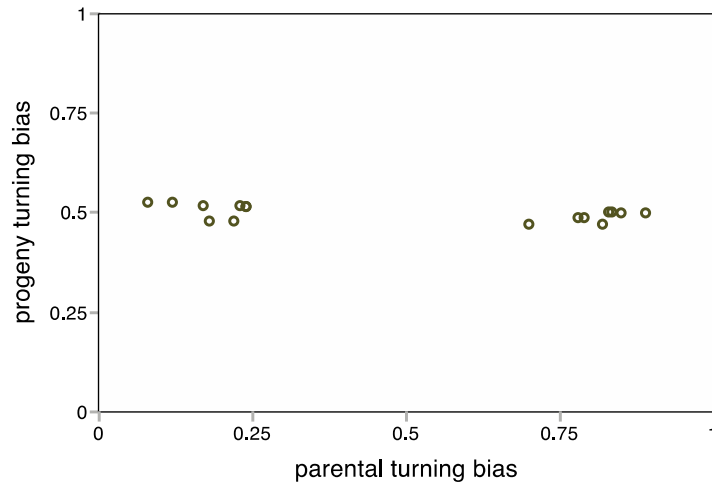|	MAD Turning Bias	MAD Number Turn	MAD Switchiness	MAD regularity of turn timing	St Dev Starvation	St Dev Chillcoma Recovery	St dev Startle Response	Night Sleep CVE
MAD Turning Bias	—	$r^2 = 0.002$, $p\text{-}val = 0.59$	$r^2 = 0.13$, $p\text{-}val <0.001$	$r^2 = 0.014$, $p\text{-}val = 0.16$	$r^2 = 0.001$, $p\text{-}val = 0.62$	$r^2 = 0.025$, $p\text{-}val = 0.06$	$r^2 = 0.013$, $p\text{-}val = 0.17$	$r^2 = 0.017$, $p\text{-}val = 0.13$
MAD Number Turn		—	$r^2 = 0.021$, $p\text{-}val = 0.09$	$r^2 = 0.006$, $p\text{-}val = 0.36$	$r^2 = 0.004$, $p\text{-}val = 0.44$	$r^2 = 0.010$, $p\text{-}val = 0.23$	$r^2 = 0.013$, $p\text{-}val = 0.18$	$r^2 = 0.000$, $p\text{-}val = 0.88$
MAD Switchiness			—	$r^2 = 0.025$, $p\text{-}val = 0.06$	$r^2 = 0.008$, $p\text{-}val = 0.29$	$r^2 = 0.021$, $p\text{-}val = 0.09$	$r^2 = 0.019$, $p\text{-}val = 0.54$	$r^2 = 0.012$, $p\text{-}val = 0.19$
MAD regularity of turn timing				—	$r^2 = 0.055$, $p\text{-}val = 0.01$	$r^2 = 0.001$, $p\text{-}val = 0.77$	$r^2 = 0.000$, $p\text{-}val = 0.96$	$r^2 = 0.011$, $p\text{-}val = 0.22$
St Dev Starvation					—	$r^2 = 0.005$, $p\text{-}val = 0.42$	$r^2 = 0.004$, $p\text{-}val = 0.47$	$r^2 = 0.001$, $p\text{-}val = 0.24$
St Dev Chillcoma Recovery						—	$r^2 = 0.002$, $p\text{-}val = 0.59$	$r^2 = 0.003$, $p\text{-}val = 0.54$
St dev Startle Response							—	$r^2 = 0.004$, $p\text{-}val = 0.47$
Night Sleep CVE								—

Fig. S3: Intragenotypic variability in various phenotypes is predominantly uncorrelated.
Scatter plots of pairs of measures of intragenotypic variability. Points are DGRP lines. Red line is linear fit with 95% confidence interval in gray. Standard deviation for starvation resistance, chill coma recovery and startle response were calculated based on data from (22). CVE for night sleep data from (23). For starvation resistance *n* per line = 40, chillcoma *n* per line = 50, startle response *n* per line = 40, night sleep *n* per line = 32.

Fig. S4: GWAS *p*-value distributions.
A.–log10(*p*-value) plotted along each chromosomal position for all SNPs. Colors and letters indicate chromosome arms **B**. QQ plot comparing observed *p*-value to a uniform distribution of expected *p*-value (lambda = 1.07).

Analysis of variance for mean turning bias

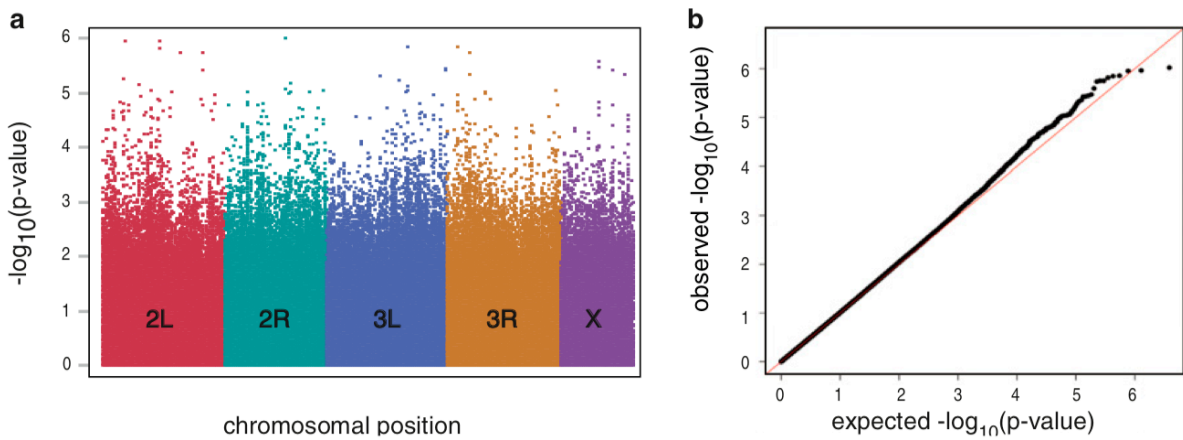| Effect	df	F	*p*
Line _{random}	158	0.88	0.85
Block _{random}	28	1.12	0.29
Line * Block _{random}	772	1	0.49
Box	5	0.41	0.84
Maze-Array	11	0.52	0.88
Box*Maze-Array	49	1.13	0.26

Analysis of variance for the absolute median deviation of turning bias

Effect	df	F	*p*
Line _{random}	158	4.31	<.00001
Block _{random}	28	0.82	0.74
Line * Block _{random}	772	1.04	0.2
Box	5	1.76	0.11
Maze-Array	11	0.67	0.76
Box*Maze-Array	49	1.16	0.22

Alternative test for heterogeneity of variance between DGRP lines for turning bias

Test	df	F	*p*
O'Brien	158	8.5953	<.00001
Brown-Forsythe	158	7.567	<.00001
Levene	158	7.701	<.00001
Bootstrap	Line specific results at online companion data page		
ANOMV	Line specific results at online companion data page		

Table S1: Statistics for analysis of mean and variance across DGRP lines for turning bias. df: degrees of freedom; F: F ratio statistic; *p*: *p*-value for F ratio statistic.

Chrs	Position	Variant	Minor Allele	Major Allele	MAF	Minor Allele Count	Major Allele Count	Mixed model Pval	Flybase ID	Gene ID	Genomic annotation
2R	13909827	SNP	C	T	0.10	15	141	9.50E-07	FBgn0034289	CG10910	UTR_3_PRIME
2L	9129764	SNP	C	G	0.05	8	145	1.09E-06	FBgn0052982	CG32982	INTRON
2L	3811210	SNP	T	C	0.11	17	140	1.11E-06	FBgn0031573	CG3407	SYNONYMOUS_CODING
3R	5804797	DEL	T	TT	0.28	40	105	1.39E-06	FBgn0263097	Glut4EF	INTRON
3L	13006450	SNP	C	A	0.17	27	129	1.42E-06	FBgn0036333	MICAL-like	SYNONYMOUS_CODING
2L	9121721	SNP	T	G	0.07	11	146	1.53E-06			
2L	16392736	SNP	T	C	0.37	52	87	1.77E-06			
3R	9419254	SNP	C	G	0.22	33	119	1.77E-06	FBgn0038159	CG14369	UPSTREAM
2L	12447996	SNP	A	T	0.40	56	85	1.84E-06	FBgn0032434	CG5421	INTRON
X	12153076	SNP	T	A	0.08	12	141	2.54E-06	FBgn0259240	Ten-a	INTRON
X	12153062	SNP	A	C	0.08	12	143	3.37E-06	FBgn0259240	Ten-a	INTRON
3L	23001316	SNP	T	C	0.08	12	144	3.54E-06	FBgn0262509	nrm	INTRON
2L	16392768	SNP	G	A	0.34	49	94	3.64E-06			
3L	23001309	SNP	A	G	0.08	12	143	3.74E-06	FBgn0262509	nrm	INTRON
X	16161192	SNP	T	A	0.35	54	100	3.75E-06	FBgn0040207	kat80	UTR_3_PRIME
X	19449711	SNP	G	A	0.06	9	149	4.38E-06			
3R	9414756	SNP	G	T	0.25	38	112	4.58E-06	FBgn0038158	CG14370	DOWNSTREAM
3L	8951894	SNP	C	G	0.22	35	121	4.77E-06	FBgn0035941	CG13313	UPSTREAM
2L	3572163	SNP	A	T	0.20	30	120	5.26E-06			
3L	11733450	SNP	A	G	0.20	30	118	5.81E-06	FBgn0036202	CG6024	INTRON
2R	14651257	DEL	AA	A	0.20	30	122	6.44E-06	FBgn0034389	Mctp	INTRON
2L	6209462	SNP	A	G	0.05	8	148	7.03E-06	FBgn0085409	CG34380	UTR_3_PRIME
3L	13006461	SNP	A	C	0.16	25	128	7.33E-06	FBgn0036333	MICAL-like	NON_SYNONYMOUS_CODING
2R	13909829	SNP	A	G	0.10	16	140	8.09E-06	FBgn0034289	CG10910	UTR_3_PRIME
2L	8003155	SNP	G	A	0.18	24	110	8.58E-06	FBgn0031972	Wwox	INTRON
3R	26478454	SNP	C	T	0.46	67	80	8.69E-06			
3L	12859591	SNP	A	G	0.17	27	128	8.82E-06			
2R	20092066	SNP	A	T	0.12	19	136	9.08E-06	FBgn0034990	CG11406	INTRON
3R	13031950	SNP	G	T	0.43	62	83	9.13E-06			
2R	17929411	SNP	G	A	0.09	14	141	9.16E-06	FBgn0005778	PpD5	SYNONYMOUS_CODING
2L	10873583	DEL	T	TGA	0.20	29	117	9.21E-06			
2R	14823241	SNP	A	G	0.07	11	144	9.26E-06	FBgn0034408	sano	INTRON
3L	12688628	SNP	T	C	0.11	17	141	9.29E-06	FBgn0014343	mirr	INTRON
2R	7130275	SNP	T	G	0.17	26	129	9.52E-06	FBgn0033593	Listericin	UPSTREAM
3R	13031960	SNP	C	A	0.42	61	85	9.85E-06			
2R	14548570	SNP	T	C	0.48	75	81	9.89E-06	FBgn0259202	CG42306	INTRON

Table S2: Top GWAS hits for MAD of turning bias.